Article

# Investigation and Application of Perforation Optimization Method on Shale Gas Horizontal Well with Numerical Simulation of Multicluster Fracturing under Dense-Segment Pattern

Chang Liu,* Haitao Li, Hongwen Luo, Yu Lu, Ying Li,* Chao Su, and Shengnan Chen

Read Online

| ACCESS | | Metrics & More | | Article Recommendations |



Modeling Theory          Simulation & Results          Field Application
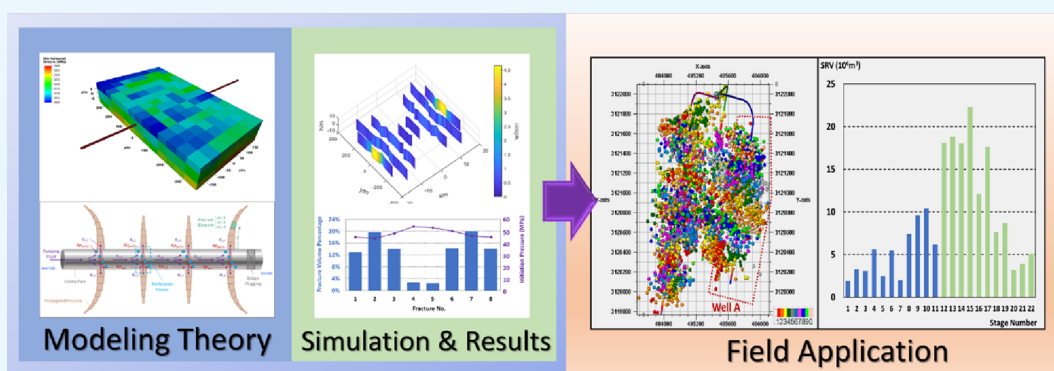
**ABSTRACT:** Multicluster fracturing of horizontal wells has evolved into a mature and widely adopted technique for exploiting unconventional oil and gas fields. A well-designed multicluster completion strategy can yield an ideal fracturing outcome, significantly enhancing production rates and potentially delivering substantial economic benefits. Nevertheless, empirical evidence suggests that fractured horizontal wells frequently exhibit pronounced nonuniform production profiles, a prevalent issue stemming from the irregular geometry of propagated fractures. This issue critically constrains production rates. To mitigate the adverse effects of low-uniformity fracture propagation, it is imperative to elucidate the factors influencing uniformity levels and their corresponding patterns. Despite extensive discussions on hydraulic fracture propagation mechanisms and optional factors in hydraulic fracturing engineering, there exists a notable oversight regarding the optimization of perforation parameters to achieve improved fracturing uniformity during well completion procedures. This paper introduces an optimization method for perforation parameters based on a fully coupled pseudo-3D numerical model of multicluster fracturing. The impact patterns of cluster spacing, perforation number, and initial perforation diameter on multifracture propagation results and uniformity levels are thoroughly examined. The multicluster fracturing model, developed using the displacement discontinuous method (DDM), is coupled with material balance, pressure transmission, hole erosion computation, and initiation asynchrony estimation. To quantify the uniformity level of the fracturing result, the modified propagation uniformity index ($U_{fm}$) is employed. Simulation results from 20 cases are categorized into six groups based on varied changing patterns of perforation parameters, leading to the identification of five recommendations for optimizing perforation parameters. By implementation of the discussed optimized perforation parameters, successful fracturing outcomes were realized.

## 1. INTRODUCTION

Hydraulic fracturing has been regarded as a major technique helping stimulate the oil and gas reservoirs.[1−5] During a hydraulic fracturing process, sand-carrying fluid is pumped into the well bore to propagate induced fractures in the formation.[6−10] Multistage fracturing and horizontal drilling are the major techniques applied in the stimulation of unconventional reservoirs such as tight sand and shale, which are hard to develop with economic benefits by normal ways due to the ultralow permeability and low porosity.[11−13] The engineering pattern of stage-by-stage simultaneous fracturing with multiple

perforation clusters has been seen as a critical stimulation method and has been proven functioning better than that with one cluster per stage in enhancing the flow abilities of oil and gas in unconventional reservoirs.[11,14] However, there is evidence

indicating an attendant problem that the profile of the inflow rates of multiple perforation clusters turns out to be nonuniform due to the poor fracture propagation uniformity, which causes the low utilization ratio of perforations and massively blocks the production potential of one fractured horizontal well.[15−22] Miller et al.'s study[23] indicates that only about 20% of the clusters contribute to the 80% of the total production by acquiring and interpreting the production logs from more than 100 horizontal shale wells in multiple basins. Coincidentally, Cipolla et al.[24] drew a similar conclusion with that above by reviewing production logs for over 100 horizontal shale-gas wells, in which less than 30% of the perforation clusters produces the most of the gas and 40% or more of the clusters are nonproductive. Another intuitive example is Luo et al.'s interpreted DTS results[25] of shale gas production inflow rates and fracture half-lengths along a horizontal wellbore with 145 fractures. In Luo et al.'s study the two profiles behave high consistency with each other and both appear low uniformities (from the interpreted data, over 61.4% noneffective perforation clusters make no contribution to both the inflow rate and fracture length).[25]

Nowadays, engineers are facing two problems: what causes the nonuniformity of the hydraulic fractures and production rate profile and how to avoid the negative effect caused by the fracture and inflow nonuniformity during a multicluster hydraulic fracturing progress.[26] To understand the factors that affect the uniformity of fracture propagation and address the associated challenges, scholars have conducted extensive research using both numerical simulations and experiments. Among the various approaches, a prevailing notion is that optimizing perforation parameters, with a specific focus on cluster spacing, can significantly enhance fracture propagation uniformity as opposed to relying solely on a manual and rigid "one-size-fits-all" approach.

A numerical simulation method has been developed from the classical mathematical modeling to investigate the complicated mechanism of fracture propagation, with the help of which many impact factors and the corresponding patterns on the fracture propagation have been concluded out. Nagel and Sanchez-Nagel[27] developed a 2D numerical model by distinct element method (DEM) to simulate the stress shadowing effect during fracturing and found that a reducing fracture spacing resulted in the increasing compressing stress field and the decreasing fracture complexity. Guo et al.[28] established a 3D planner fracture propagation model based on finite-element method (FEM) to simulate the multifracturing and optimize the cluster spacing for a stage example to get a high level of fracture uniformity, and the simulation also considered significantly the stress shadow effect. Zhao et al.[29] investigated the process of simultaneous fracture propagations and measures to improve the fracture growing uniformity by building a pseudo 3D boundary element model (BEM) using the displacement discontinuous method (DDM), concluding that adjusting the fluid partitioning and balancing the stress interference such as interwell stress interference are the effective measures to promote the fracture growth uniformity. However, Zhao et al.'s study[29] did not mention how to design actual engineering to properly adjust the fluid partitioning. Wang[30] presented a fully coupled hydraulic fracturing model using cohesive zone method (CZM), which was based on the extended finite element method (XFEM), and studied how the fracture spacings under different fracturing sequence patterns controlled the fracture competition against each other. The predominant approaches

have greatly advanced numerical modeling capabilities and expanded our understanding of multifracturing mechanisms. This, in turn, facilitates further investigation into the effects of additional perforation parameters on fracture propagation uniformity, going beyond just fracture spacing or cluster intervals.

Not only do the stress fields altered by fractures of different spacing values have a critical impact on the propagation process but the pressure differences between the fractures and the casing pipe can also play a significant role in varying the fracture volume distribution. The limited-entry method has become a widely used technique in completion design for the fracturing wells, whose general principle is to generate the uneven extra entry frictions and redistribute the fluid injection volumes into each fracture by cutting down partially or entirely the perforation numbers of the chosen clusters, as a result of which the stress interference among fractures can be potentially counteracted and a uniform fracturing result can be expected.[31−36] Li et al.[16] employed a 3D hydro-mechanical coupled finite element model and illustrated the impact of limited-entry designed perforation parameters, including the perforation number and stress shadowing on the simultaneous propagation of multiple fractures. Li et al.[16] concluded that it is possible to counteract the stress shadow effect and improve the total fracture area by increasing the perforation friction pressure or applying the uneven perforation number strategy. Lu et al.[37] presented a 2D nonplanner coupled numerical model and studied the impact of different completion schemes on multiple fracture growth, which contains both the evenly and unevenly distributed cluster spacings, perforation numbers, and perforation diameters. Lu et al.'s study[37] has given a comprehensive understanding on how the completion strategies with variety of perforation parameters influence the multifracturing effect. However, the cluster and perforation numbers used in Li et al.[16] and Lu et al.'s[37] modeling cases appear to be fewer than those practically adopted in the field stimulation designs in recent years. Also, numerical studies neglect the erosion of perforation holes and the fracture initiation asynchrony effect, which are both commonly encountered phenomena in field engineering. Thus, there remains a wide space of studies on both function strengthening of numerical modeling and enrichment of perforation parameter cases.

Although in many research studies, the mechanism of the hydraulic fracture propagation and factors influencing the fracture uniformity have been richly discussed, it seems that there remains a neglected point of view on the optimization of perforation parameters. Based on the numerical modeling method, this paper presents how the perforation parameters impact the propagation uniformity level of multicluster fracturing under varied completion strategies and forms a theoretical guidance for the purpose of an ideal hydraulic fracturing effect and the satisfied production rates of unconventional reservoir wells. In this study, a fully coupled pseudo 3D model of multicluster fracturing is built to simulate the simultaneous fracture propagation within a single stage. The model is built based on the DDM (displacement discontinuity method), which is a kind of indirect boundary element model that has been frequently used and well tested in other previous studies, and an algorithm of the perforation erosion effect is coupled into the model. In addition, to simulate the fracturing results at different perforation strategies, the other coupled modules are added into the model including those of material balance, the pressure transmission, the hole erosion computa-
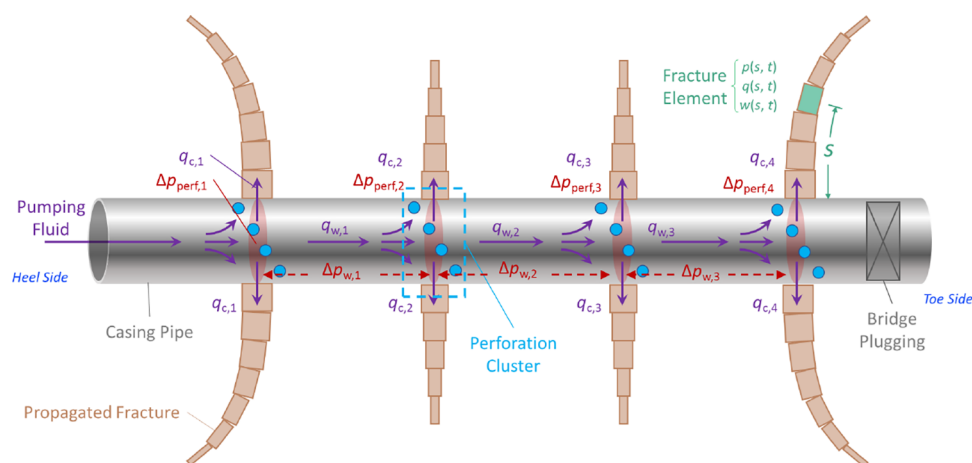
**Figure 1.** Pressure transmission system coupled with fracture propagation model built by DDM (displacement discontinuity method) for a four-cluster perforation example.

tion, and the initiation asynchrony estimation. Meanwhile, the propagation uniformity index $U_{\text{fm}}$ is employed to quantify the uniformity level of the fracturing result, and the value's $U_{\text{fm}}$ is calculated by the formula modified based on Lu et al.'s work.[37] Moreover, simulation results of 20 cases in total are presented to analyze the relationships between the distribution patterns of three types of perforation parameters (the cluster spacing, the perforation number, and the initial perforation diameter) and propagation uniformity indices, among which the densely segmented fracturing cases (four limited-entry cases and three extreme limited-entry cases) are included.

In cases where numerous pre-existing natural fractures are present in the formation, the geometry of the propagated fractures forms a complex network, making it challenging to assess their uniformity. However, it is nearly impossible for today's techniques to give a completed and precise measurement of the fracture network as the standard for fracturing quality evaluation.[38] Considering that this paper is focusing on perforation optimization, the relationship between the quality of fracture network and the well completion is not the key point to discuss in this work but could be a good problem to be investigated in future research.

The simulation results of the 20 cases are divided into 6 groups by different change patterns of perforation parameters, from which 5 advices of how to optimize the perforation parameters are concluded.

## 2. NUMERICAL MODELING

**2.1. Model Assumptions.** The numerical multicluster fracturing model can simulate the simultaneous propagation of multiple fractures from the perforation clusters within a single horizontal stage of the treatment wellbore. In the model, the fractures are designed as pseudo 3D displacement discontinuous elements with elastic mechanical properties, whose total number should increase with fracture propagating time. The horizontal section of the well trajectory is considered drilling in the same direction with the average minimum horizontal principal stress with no vertical inclination. The fracture treating fluid, regarded as incompressible, is pumped through a single casing pipe that functions as the only treatment tube for a simple consideration. The formation matrix consists of one single layer or several layers of cubic grids containing the rock mechanical and physical in situ properties and can be set as either a homogeneous or a

heterogeneous network. In this paper, data referring to the shale reservoir Y at southwest of China are employed to build the numerical strata matrix model, which is a three-layer structure with a homogeneous minimum horizontal stress distribution and used to simulate one fracturing stage. The well path is located in the middle layer, and the fracture treating fluid is injected. The well stage in the model is built using the data of well A, which is a horizontal producing well to be completed in reservoir Y. From top to bottom, the layer thicknesses are 6, 10, and 7 m, and the average minimum horizontal stresses are 72, 70, and 73 MPa. The wellbore trajectory is located at the middle layer with the thickness of 10 m and the average horizontal stress of 71.6 MPa.

There are four boundary conditions considered in the fracturing model: (a) the width of each fracture tip element is 0; (b) the pressure within each fracture tip element equals the in situ closure stress; (c) the flow-out rate of each fracture tip element is 0; (d) the first element of each fracture, which directly connects the borehole, has the same amount of flow-in rate with that of the fluid rate flowing into the corresponding perforation cluster. In addition, the entire model is initiated with 0 length of each fracture.[38,39]

**2.2. Material Balance.** At each time point in the fracturing progress, the flow rate of a single fracture element must always satisfy the material balance law, as shown in Figure 1. Within a unit time-step, the flow-in fluid volume of a certain fracture element equals to the sum of the fracture element volume increment due to the increasing width, the leak-off fluid volume through the fracture wall, and the flow-out fluid volume from this fracture element, which can be expressed by[38]

$$\int_{t-\Delta t}^{t} q_{\text{in}}(t)\,dt = \int_{t-\Delta t}^{t} ah\Delta w(t)\,dt + \int_{t-\Delta t}^{t} q_{\text{L}}(t)\,dt + \int_{t-\Delta t}^{t} q_{\text{out}}(t)\,dt \tag{1}$$

where $q_{\text{in}}$, $q_{\text{out}}$, and $q_{\text{L}}$, all related to time, are the fluid flow-in rate, flow-out rate, and leak-off rate of the given element, respectively. Moreover, $a$, $h$, and $\Delta w$ are the length, height, and time-related width increments of the fracture element, respectively. $t$ refers to the time that the fracture propagation progress experiences in the simulation. $\Delta t$ refers to the unit time of the discrete propagation time. When the $\Delta t$ value was set larger, the computation would get faster while the simulation

result could be less accurate. $\tau$ is the initial time when the corresponding fracture element starts to be exposed to the fluid. In this way, $t - \tau$ is the time that the leak-off progress of the corresponding fracture element experiences. The fluid leak-off rate can be calculated using Carter leak-off model,[40] which is described as

$$q_L(t) = 2hC_L(t - \tau)^{-0.5} \tag{2}$$

in which $C_L$ is the leak-off coefficient and $\tau$ is the time the fracture element exposes to the fluid.

**2.3. Pressure Transmission.** The entire system of fluid pressure transmission in the model mainly consists of the following three parts: the pressure transmissions in the fractures, the pressure differences existing at the perforation clusters due to the entry frictions, and the pressure drop along the casing pipe in the target stage of the horizontal wellbore. A four-cluster stage example of a comprehensive pressure system is presented in Figure 1.

First, the pressure transmission within each fracture is governed by Poiseuille's law, which can be expressed as[41,42]

$$\frac{\partial p(s, t)}{\partial s} = -\frac{64\mu}{\pi h w^3(s, t)} q(s, t) \tag{3}$$

where $p(s, t)$, $q(s, t)$, and $w(s, t)$ are the time-related fracture pressure, fluid flow rate, and fracture width at the point of distance $s$ from the wellbore, respectively.

In addition, the pressure difference between the casing pipe and the fracture at each perforation cluster is generated due to the fluid entry friction and can be described as the following equation:[31,43]

$$\Delta p_{\text{perf}} = 0.807 \frac{q_c^2 \rho}{n_{\text{perf}}^2 d_{\text{perf}}^4 C_d^2} \tag{4}$$

in which, $\Delta p_{\text{perf}}$, $n_{\text{perf}}$, and $d_{\text{perf}}$ are the pressure difference, perforation number, and average perforation diameter of the given cluster, respectively. In addition, $q_c$ stands for the total fluid rate passing through the perforation holes of the given cluster. $\rho$ is fluid density, and $C_d$ is discharge coefficient. Typically, a $C_d$ of 0.6 is assumed for new perforations, and a value of 0.85 is assumed for fully eroded perforations.

Meanwhile, the friction between the fluid and the casing pipe wall causes the pressure drop along the casing pipe, which can be expressed as[44]

$$\Delta p_{w,i} = C_w L_{w,i} q_{w,i} \tag{5}$$

in which, $\Delta p_{w,i}$, $L_{w,i}$, and $q_{w,i}$ are the fluid friction pressure, well length, and fluid flow rate of the cluster interval between the no. $i$ cluster and the no. $(i + 1)$ cluster, respectively. The pressure-drop coefficient $C_w$ depends on the flow pattern of the fracturing fluid and can be calculated with the following equation:

$$C_w = \begin{cases} 2^{3n'+2} \pi^{-n'} k' \left( \frac{1 + 3n'}{n'} \right) d_w^{-(3n'+1)}, & \text{(power law fluid)} \\ \frac{128\mu}{\pi d_w^4}, & \text{(Newtonian fluid)} \end{cases} \tag{6}$$

where $n'$ and $k'$ are the flow behavior index and consistency coefficient of the power law treating fluid, respectively. When the treating fluid is regarded as a Newtonian fluid, $n'$ equals to 1 and

$k'$ becomes the viscosity $\mu$. $d_w$ is the casing inner diameter, which remains constant within a given stage.

The three parts of the pressure system directly govern the fluid injection separation in each fracture, which has a remarkable influence on the fracture propagating uniformity. According to eq 4, the pressure difference of one cluster turns out to be adjustable by changing the perforation number of one cluster and perforation diameters. However, it should be taken into consideration that the perforation diameters and the discharge coefficient would change due to hole erosion during proppant pumping progress, which could possibly cause a non-negligible error in the final simulation result.

**2.4. Elastic Propagation.** When fracturing fluid starts to be pumped into the well, fractures will initiate from multiple clusters and then generate an induced stress field altering the in situ horizontal stress field, which further influences the fracture propagating direction in the rock matrix. This behavior is considered in the numerical model, which is built by the theory of displacement discontinuity method. The new stress field around the fractures at each time point can be expressed as[45]

$$\begin{cases} \sigma_n^i = \sum_{j=1}^{N} G^{ij} C_{ns}^{ij} D_s^j + \sum_{j=1}^{N} G^{ij} C_{nn}^{ij} D_n^j \\ \sigma_s^i = \sum_{j=1}^{N} G^{ij} C_{ss}^{ij} D_s^j + \sum_{j=1}^{N} G^{ij} C_{sn}^{ij} D_n^j \end{cases} \tag{7}$$

where $\sigma_n^i$ and $\sigma_s^i$ are total normal and shear stress components, which are generated by all the existing fracture elements, applied on the $i^{\text{th}}$ fracture discrete element. $D_s^j$ and $D_n^j$ are normal and shear displacement discontinuities of the $j^{\text{th}}$ fracture discrete element. The elastic mechanical factors $C_{ns}^{ij}$, $C_{nn}^{ij}$, $C_{ss}^{ij}$, $C_{sn}^{ij}$ and $G^{ij}$ can be respectively derived with the formulas given by Crouch et al. and Olson,[45,46] the calculation of which can reference eqs 8−10. $N$ is the total number of the fracture discrete elements at a given time point. $x_i$, $y_i$, $x_j$, and $y_j$ are the global coordinate values of the $i^{\text{th}}$ and the $j^{\text{th}}$ fracturer unit. $\bar{x}$ and $\bar{y}$ are the relative coordinate values of the $i^{\text{th}}$ fracturer unit in the local coordinate system whose origin is located at the center point of the $j^{\text{th}}$ fracturer unit. $\beta_j$ is the angle between the $\bar{x}$ direction and the $x$ direction. $a$ is the half-life of the fracture unit. Figure 2 gives a direct understanding of the relative position between any two fracture units and the physical descriptions of the variables above.
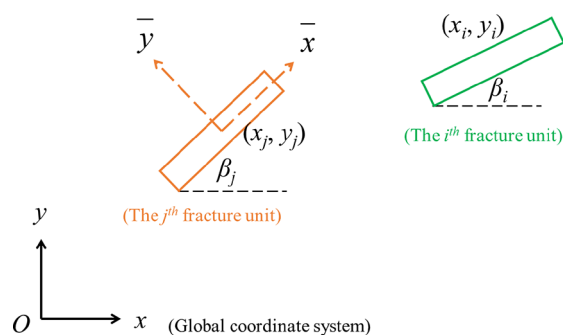


**Figure 2.** Schematic of the relative position between the $i^{\text{th}}$ fracture unit and the $j^{\text{th}}$ fracture unit. The origin of the global coordinate system is set at the center point of the wellbore stage.

$$\begin{cases} C_{ns}^{ij} = 2\left[2f''_{xy}\sin^2\beta_j + f''_{xx}\sin2\beta_j - \overline{y}\Big(f''_{xyy}\cos2\beta_j \right. \\ \qquad\qquad \left. + f''_{yyy}\sin2\beta_j\Big)\right] \\[4pt] C_{nn}^{ij} = 2\left[ -f''_{xx} + \overline{y}\Big(f''_{xyy}\sin2\beta_j - f''_{yyy}\cos2\beta_j\Big)\right] \\[4pt] C_{ss}^{ij} = 2\left[2f''_{xy}\cos^2\beta_j - f''_{xx}\sin2\beta_j + \overline{y}\Big(f''_{xyy}\cos2\beta_j \right. \\ \qquad\qquad \left. + f''_{yyy}\sin2\beta_j\Big)\right] \\[4pt] C_{sn}^{ij} = 2\left[ -f''_{xx} - \overline{y}\Big(f''_{xyy}\sin2\beta_j - f''_{yyy}\cos2\beta_j\Big)\right] \end{cases}$$

(8)

$$\begin{cases} f'_x = \dfrac{1}{4\pi(1-\nu)}\Big\{\ln[(x-a)^2+y^2]^{1/2} \\ \qquad\qquad - \ln[(x+a)^2+y^2]^{1/2}\Big\} \\[8pt] f'_y = -\dfrac{1}{4\pi(1-\nu)}\left[\arctan\dfrac{y}{x-a} - \arctan\dfrac{y}{x+a}\right] \\[8pt] f''_{xx} = \dfrac{1}{4\pi(1-\nu)}\left[\dfrac{x-a}{(x-a)^2+y^2} - \dfrac{x+a}{(x+a)^2+y^2}\right] \\[8pt] f''_{xy} = \dfrac{1}{4\pi(1-\nu)}\left[\dfrac{y}{(x-a)^2+y^2} - \dfrac{y}{(x+a)^2+y^2}\right] \\[8pt] f''_{yy} = -\dfrac{1}{4\pi(1-\nu)}\left[\dfrac{x-a}{(x-a)^2+y^2} - \dfrac{x+a}{(x+a)^2+y^2}\right] \\[8pt] f'''_{xyy} = \dfrac{1}{4\pi(1-\nu)}\left[\dfrac{(x-a)^2-y^2}{[(x-a)^2+y^2]^2}\right. \\ \qquad\qquad \left. - \dfrac{(x+a)^2-y^2}{[(x+a)^2+y^2]^2}\right] \\[8pt] f'''_{yyy} = \dfrac{2y}{4\pi(1-\nu)}\left[\dfrac{x-a}{[(x-a)^2+y^2]^2}\right. \\ \qquad\qquad \left. - \dfrac{x+a}{[(x+a)^2+y^2]^2}\right] \end{cases}$$

(9)

$$\begin{cases} \overline{x} = (x_i - x_j)\cos\beta_j + (y_i - y_j)\sin\beta_j \\ \overline{y} = -(x_i - x_j)\sin\beta_j + (y_i - y_j)\cos\beta_j \end{cases}$$

(10)

The maximum circumferential stress criterion can be described as in equation 11:

$$0.5\left[\cos\frac{\theta_f}{2}K_I\Big(1+\cos\theta_f\Big) - 3K_{II}\sin\theta_f\right] > K_{IC}$$

(11)

in which $\theta_f$ is fracture tip deflection angle. $K_{IC}$ is the fracture toughness value of the rock matrix. $K_I$ and $K_{II}$ are the mode I stress-intensity-factor and mode II stress-intensity-factor, respectively, which can be determined by eqs 12 and 13:[47,48]

$$K_I = \frac{0.806E\sqrt{\pi}}{4(1-\nu^2)\sqrt{2a}}D_n$$

(12)

$$K_{II} = \frac{0.806E\sqrt{\pi}}{4(1-\nu^2)\sqrt{2a}}D_s$$

(13)

where $E$ and $\nu$ are Young's modulus and Poisson's ratio. $a$ is the half length of the fracture tip element. $D_n$ and $D_s$ refer to the normal and shear displacement discontinuities of the tip element.

When eq 11 is satisfied, the fracture tip would continue to propagate and simultaneously turn at a certain deflection angle, which is determined by eq 14:[49]

$$K_I\sin\theta_f + K_{II}(3\cos\theta_f - 1) = 0$$

(14)

The following equation is established to decide the relationship between fracture weight and fracture height, which is modified based on the equilibrium height growth model proposed by Zhao et al.:[29]

$$w = \frac{h(1-\nu^2)}{E}\left(\sqrt{\frac{\pi}{2h}}K_{IC}\Big(\frac{H}{h}\Big)^{\frac{3}{2}} + \Delta\sigma_c\sqrt{\frac{H^2}{h^2}-1}\right)$$

(15)

in which $w$ and $H$ are the fracture width and modified fracture height. $h$ is the height of formation layer within which fractures initiate and is assumed to be the fracture height before modification. $\Delta\sigma_c$ is the closure stress difference between the fracture formation layer and its vertically adjacent layer. By practical computation in our model, it is found that the fracture height is easily trapped within its located formation layer due to layer variation.

**2.5. Initiation Asynchrony.** The fracture shape uniformity is influenced by not only the uneven inflow rate distribution but also the asynchronous initiation progress as well. Ideally, all of the fractures would simultaneously initiate when fluid is pumped into the well. However, the fact is that some of the perforation clusters would potentially behave a delay on fracture initiation or even turn out to be noneffective perforation clusters generating no fractures at all because of the impact from the formation matrix heterogeneity along the wellbore and the fracture stress shadow effect, which is a classical problem that is encountered by the field engineers. Thus, it is necessary to consider the lateral heterogeneity and simulate the initiation asynchrony phenomenon in the model, or the final fracture uniformity level could be remarkably overestimated. The fracture initiation estimation step is added before the propagation step in the model which can judge whether the fracture would initiate or not at each perforation cluster and, if yes, when the fracture initiate. The fracture initiation estimation step should always be executed before the fracture propagation simulation at any time-step whenever there remain clusters with no fractures.

To start the estimation, the breakdown pressure at each perforation cluster is computed based on the input in situ stress profile data and M.M. Hossain et al.'s formulas, which are described as[50]

$$P_{w0} = \frac{1}{4}[9\sigma_H - \sigma_h - 3\sigma_v + 2\nu(\sigma_v - \sigma_H)]$$

(16)

$$P_{w90} = \frac{1}{4}[9\sigma_v - \sigma_h - 3\sigma_H + 2\nu(\sigma_v - \sigma_H)]$$

(17)

$$P_{wf} = \min(P_{w0}, P_{w90})$$

(18)
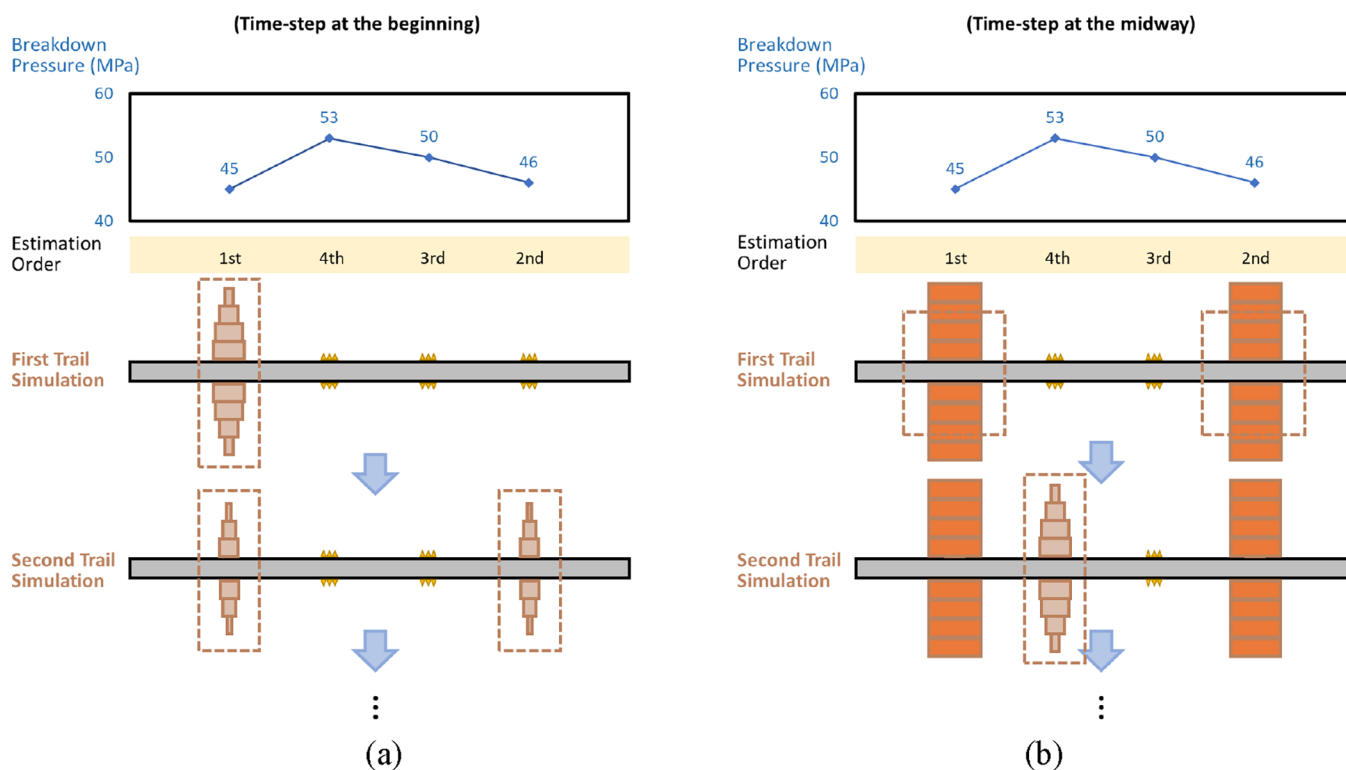
**Figure 3.** Schematic of trial simulation processes of the fracture initiation estimation at 2 types of simulation time-steps in a four-cluster stage, where the fracture forms in each trail simulation is not the actual final result at that time-step. (a) Estimation at the beginning time-step and (b) at the midway time-step.

where $P_{w0}$ and $P_{w90}$ are breakdown pressures of perforations with the phase angles of 0 and 90°. $\sigma_v$ is the in situ vertical stress. $P_{wf}$ is the breakdown pressure of the given perforation cluster. Moreover, before the simulation of the fracture propagation at each time-step, all the noninitiated perforation clusters are recognized and ordered by the corresponding breakdown pressures from low to high. This order is prepared for the fracture initiation estimation, which is a trial-and-error procedure rather than the actual fracture initiation order because it likely happens that the fractures with similar breakdown pressures simultaneously initiate and there is no such an initiation order between them. Figure 3 presents the schematic of fracture initiation estimation processes at two types of simulation time-steps in a four-cluster stage with the breakdown pressures of perforation clusters and the corresponding estimation order. FigurE 3a presents the estimation at the very beginning time-step of the entire simulation; the trail simulation runs with only one effective perforation cluster having the lowest breakdown pressure, i.e., the first cluster in the estimation order. The trail simulation is based on the model coupled with the governing equations in Sections 2.1 to 2.5. An adequate bottomhole pressure at a certain cluster is required to keep the demanded fluid pumping rate through the perforation holes. The bottomhole pressures are normally varied at different perforation clusters, and once it happens at any of the other noninitiated clusters that the computed bottomhole pressure exceeds the breakdown pressure, the trail simulation of this time-step would restart with one more effective perforation cluster having the second lowest breakdown pressure. Finally, the trail-and-error circulation of the fracture initiation estimation ends until the entire pressure system balance is reached. A similar process of the initiation estimation at the midway time-step is

presented in Figure 3b, in which the first trial simulation runs with the clusters that have already initiated, and then the bottomhole pressures and the breakdown pressures at all the noninitiated clusters are compared. Figure 4 presents the flowchart of initiation asynchrony progress, as indicated by which the trail simulations should always be executed at every
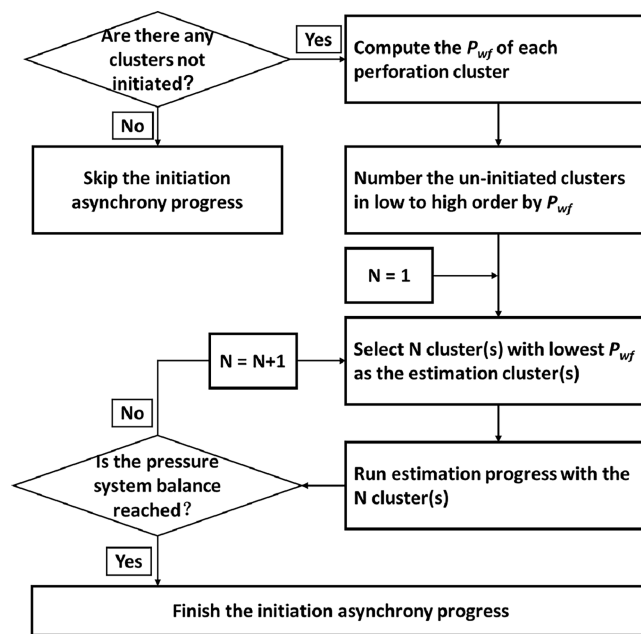


**Figure 4.** Flowchart of the initiation asynchrony progress, which is executed before the fracture propagation computation at each time-point whenever there exists clusters uninitiated.

time-step during the entire simulation unless all the perforation clusters get initiated.

**2.6. Hole Erosion.** Hole erosion happens when pumping slurry flows through the perforation hole into the fracture, as a result of which, the eroded edge will lead to the simultaneous increases in both the hole diameter and discharge coefficient.[51] The relationship between hole diameter, discharge coefficient, and time can be described as eqs 19 and 20 according to Cramer's experiment result:[52]

$$d_{\text{perf}} = \left( \frac{80\alpha\eta q_c^2 t}{n_{\text{perf}}^2 \pi^2} + d_{\text{perf0}}^5 \right)^{0.2} \tag{19}$$

$$\frac{\partial C_d}{\partial t} = \eta\beta v^2 \left( 1 - \frac{C_d}{C_d^{\max}} \right) \tag{20}$$

in which $\alpha$ and $\beta$ are two independent perforation erosion parameters and can be obtained by matching Cramer's laboratory data. $\eta$ is the proppant concentration. $v$ is the fluid flow velocity through a single perforation hole.

According to the research of Barree,[53] the perforation holes typically erode between 0.004−0.008 in per 1000 lb (453.59 kg). If a typical limited entry design is deployed with ideal sand distribution, the size of each perforation would increase by 20−40% because of the erosion.[54]

## 3. RESULTS AND DISCUSSION

It is believed that with the more uniform fractures result in the higher stimulated reservoir volume and the larger area of the reservoir connected with fractures, to reach the goal of which a reasonable design of hydraulic fracturing needs to be seriously concerned.[29,37,55,56] However, besides the applicable fracturing treatment schedule, optimization of the cluster perforation parameters trend to be non-negligible in today's hydraulic fracturing design for the purpose of creating uniform fractures, including the techniques of limited-entry perforation and extreme limited-entry perforation, which have been globally used in stimulations of unconventional oil and gas reservoirs. Based on the numerical model built in Section 2, this section presents the estimation of fracture propagating uniformities impacted by the cluster perforation parameters including the cluster spacing, perforation number per cluster, and the perforation diameter, which are either evenly or unevenly distributed along the wellbore. With the help of the multicluster fracturing model, the fracturing simulation results of the horizontal well A under different perforation schedules are presented and discussed. For the sake of a clear way to estimate the fracturing simulation results, the fracture propagating uniformity in each simulation case is quantized as the modified fracture uniformity index, which is expressed as

$$U_{fm} = 1 - \frac{N \sum\limits_{i=1}^{N} |V_i - \bar{V}|}{2(N-1) \sum\limits_{i=1}^{N} V_i} \tag{21}$$

where $V_i$ and $\bar{V}$ are respectively the single fracture volume from the $i^{\text{th}}$ cluster and the average fracture volume within the target stage. $N$ is the total number of fractures. The modified fracture uniformity index $U_{fm}$ is between 0 and 1. The $U_{fm}$ value closer to 1 indicates better fracture propagating uniformity. Equation 21

is modified based on Lu et al.'s paper[37] in which the uniformity index $U_f$ is expressed as the relative mean deviation of the fracture volumes within a stage. The advantage of the modified uniformity index applied in this paper is that the impact of the total number of fractures is concerned. Specially, the "fracture uniformity index" terms in this paper all refer to the modified fracture uniformity index $U_{fm}$ without any declarations.

Table 1 gives the general input parameters used in all of the modeling cases, and Table 2 lists the detailed modeling cases

### Table 1. General Input Data of Modeling Cases

| parameter | value | unit |
|---|---|---|
| Young's modulus | 45 | GPa |
| Poisson's ratio | 0.25 | |
| average minimum horizontal stress | 70 | MPa |
| average maximum horizontal stress | 84 | MPa |
| average depth of the fractured layer | 2042 | m |
| formation pressure gradient | 0.027 | MPa/m |
| height of hydraulic fractured layer | 10 | m |
| injection rate | 14 | m³/min |
| fluid viscosity | 2 | mPa·s |
| fluid density | 1100 | kg/m³ |
| proppant concentration | 413 | kg/m³ |
| casing pipe diameter | 0.139 | m |
| stage length | 66 | m |

with various factors influencing the fracture uniformity index. The data in Table 1 are employed referring to the shale reservoir Y. There are 20 eight-cluster modeling cases in total to be presented which are divided into six groups by influencing

### Table 2. List of Modeling Cases (Eight Clusters)

| case | clusterspacing (m) | perforation number | initial perforation diameter (mm) | parameter distribution |
|---|---|---|---|---|
| a-1 | 5 | 16 | 7 | even |
| a-2 | 8 | 16 | 7 | even |
| a-3 | 12 | 16 | 7 | even |
| a-4 | 15 | 16 | 7 | even |
| b-1 | 5\|5\|8\|8\|12\|12\|15 | 16 | 7 | uneven |
| b-2 | 5\|5\|15\|15\|15\|5\|5 | 16 | 7 | uneven |
| b-3 | 5\|8\|12\|15\|12\|8\|5 | 16 | 7 | uneven |
| b-4 | 5\|15\|5\|15\|5\|15\|5 | 16 | 7 | uneven |
| c-1 | 5 | 8 | 7 | even |
| c-2 | 5 | 4 | 7 | even |
| c-3 | 8 | 8 | 7 | even |
| c-4 | 8 | 4 | 7 | even |
| d-1 | 8 | 2_2_2_3_3_4_4_4 | 7 | uneven |
| d-2 | 8 | 2_2_2_3_3_3_3_3 | 7 | uneven |
| d-3 | 8 | 2_2_2_3_3_2_2_2 | 7 | uneven |
| e-1 | 8 | 16 | 10 | even |
| e-2 | 8 | 16 | 14 | even |
| f-1 | 8 | 16 | 7_7_7_14_14_7_7_7 | uneven |
| f-2 | 8 | 16 | 14_14_14_7_7_14_14_14 | uneven |
| f-3 | 8 | 16 | 7_7_7_10_10_14_14_14 | uneven |

(a)

(b)
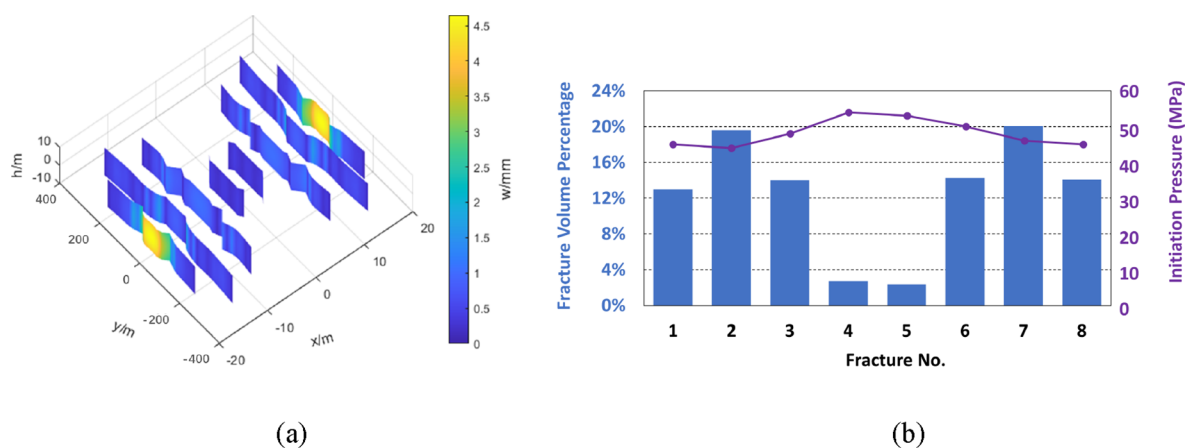
**Figure 5.** 3D view (a) and fracture volume distribution (b) of the eight-cluster modeling result case a-1, in which the evenly distributed cluster spacing is 5 m and the perforation numbers are all 16 per cluster.



Case a-2                                    Case a-3                                    Case a-4
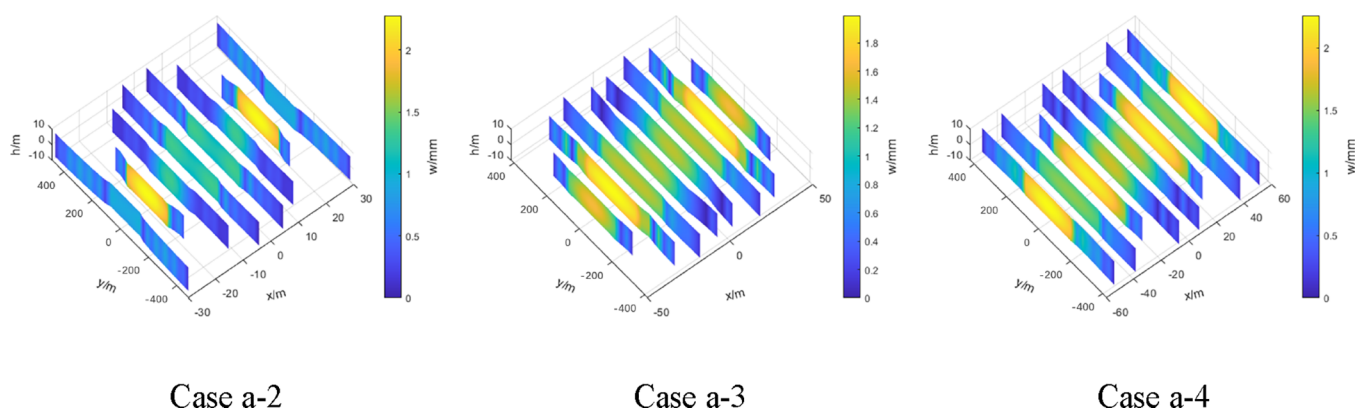
**Figure 6.** 3D views of case a-2 to case a-4 modeling results.



Case a-1          Case a-2          Case a-3          Case a-4
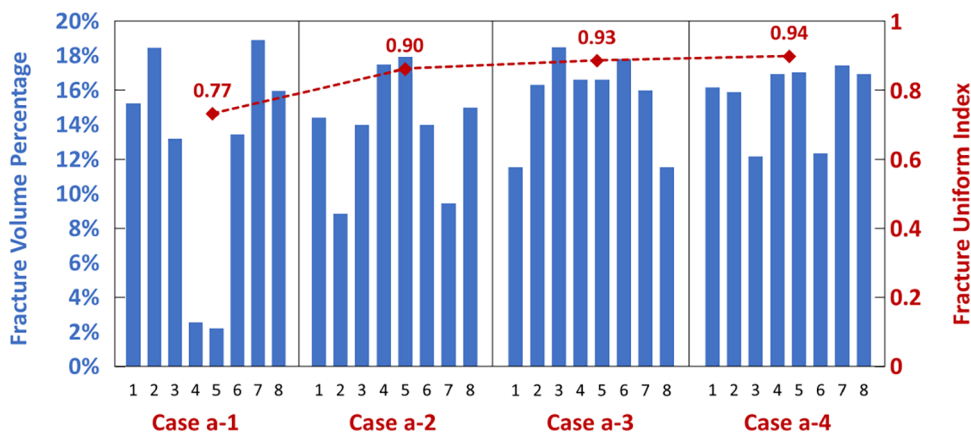
**Figure 7.** Distributions of fracture volume percentages and fracture uniformity indices of case a-1 to case a-4 with evenly distributed cluster spacings, of which the cluster spacings are 5, 8, 12, and 15 m, respectively.

factors to be analyzed individually. For the cases in Table 2, each parameter is set as either a single value or a character string composed of values and symbols. The single values represent the evenly distributed parameter values set for all of the clusters in the corresponding cases. The unevenly distributed values separated by short vertical bar symbols or short underline symbols represent unevenly distributed parameter values. The short vertical bar symbols represent the clusters, and the short underline symbols represent the spacings between any two adjacent clusters. Among a certain character string, the most left

number indicates the parameter value set for the first cluster or cluster spacing within the stage counted from the toe side of the wellbore.

**3.1. Single Case Analysis.** There are eight clusters in the modeling case a-1 with seven evenly distributed spacings of 15 m, and each cluster is set with 16 perforation holes. It is clear from 5a that fractures close to the stage center are shorter than the others. 5b displays the fracture volume percentage differences between the eight fractures and the related initiation pressure, in which the no. 1 fracture corresponds to the first

Case b-1



Case b-2



Case b-3



Case b-4
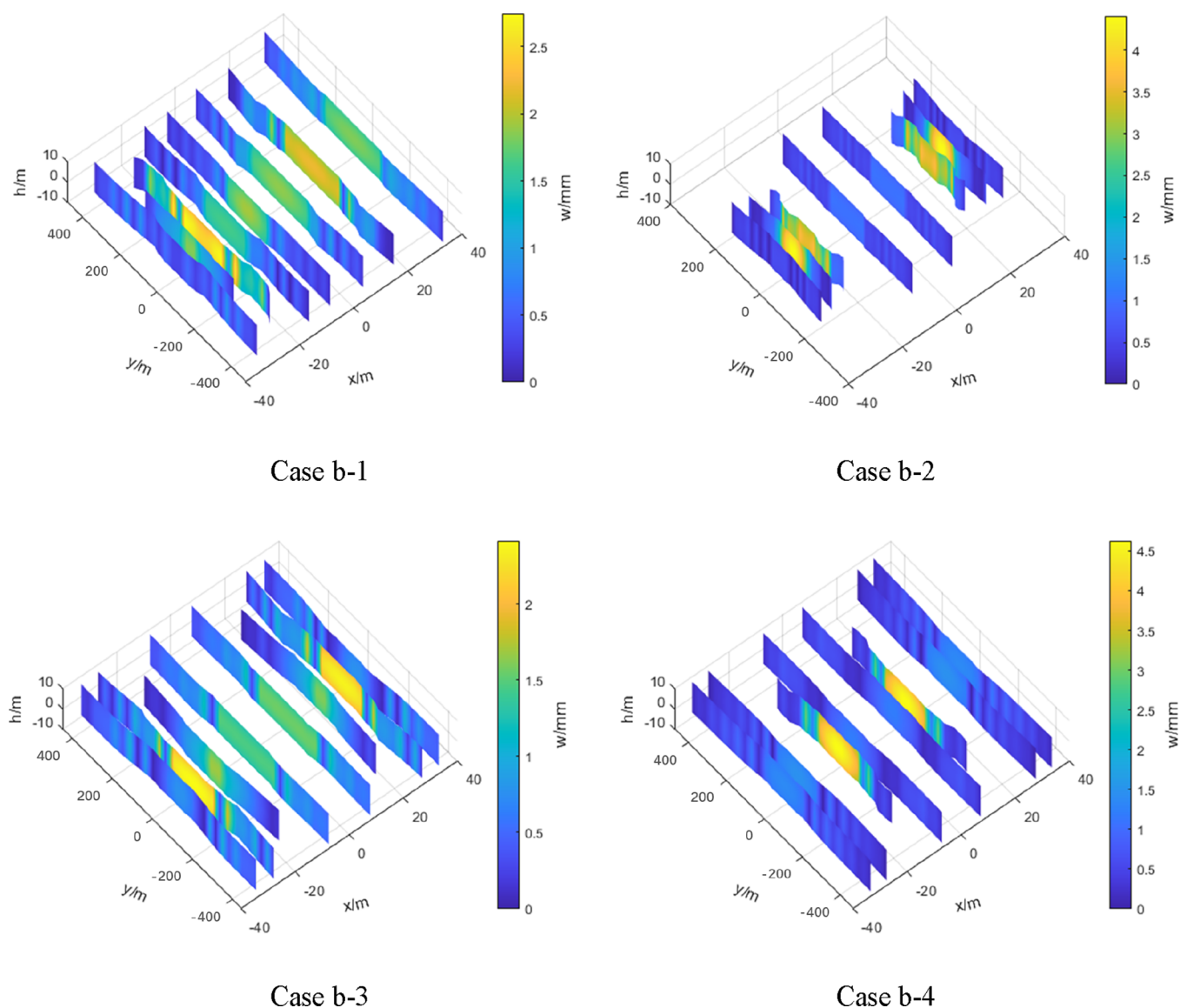
**Figure 8.** 3D views of cases b-1 to b-4 modeling results.

fracture counted from the heel side of the wellbore and the no. 8 fracture is the closest to the toe side. In Figure 5, the no. 4 and no. 5 fractures with the highest initiation pressures suffer the strongest resistance effect during propagating for not only the stress shadow effect but more significantly the initiation asynchrony. The fracture uniformity index $U_{fm}$ of case a-1 is 0.77, which indicates that there is still a potential to optimize the cluster perforation design to obtain more uniform fracture propagation.

**3.2. Cluster Spacing.** Cases of a-1 to a-4 are taken as a group to help analyze the influence of varied even cluster spacings on the fracture uniformity index $U_{fm}$. The perforation numbers in the 4 cases are set the same as 16 per cluster and the initial perforation diameters are all 7 mm. The cluster spacing of cases a-1 to a-4 are set as 5, 8, 12, and 15 m, respectively, among which 5 and 8 m can be identified as densely segmented perforation. From the simulation results and fracture uniform indices of cases a-1 to a-4, as presented in 6 and 7, it can be found that the gradually enlarged cluster spacings result in the increased fracture uniformity index and weakening diversity of fracture volume distribution. The reason is that the closer fracture

spacing generates the heavier stress interference, which causes the higher extra closure pressure applied on the central fractures with a preventing effect on fracture propagation. Under the condition of even-distribute cluster spacing, an enlarged spacing can improve the fracture uniformity index by over 20%. However, when the spacing adds to a certain degree the impact on the fracture uniformity index gets limited. As indicated in 6, the fracture uniformity index increment from case a-3 to case a-4 can be almost neglected.

In order to investigate how the uneven-distributed cluster spacings influence the fracture uniformity index, four types of distribution modes of cluster spacings are established and used in the cases of b-1 to b-4. In case b-1, the clusters are arranged in an increasing order from the heel side to the toe side, which is "5 | 5 | 8 | 8 | 12 | 12 | 15". In case b-2, the distribution mode of "wide in center but narrow on sides" is applied, which is "5 | 5 | 15 | 15 | 15 | 5 | 5". In case b-3, the cluster spacings arrange in the mode of "decreasing from center to two sides", which is 5 | 8 | 12 | 15 | 12 | 8 | 5. For case b-4, the cluster-spacings distribute in the mode of "circulation with a large one and a small one", which is "5 | 15 | 5 | 15 | 5 | 15 | 5". Figures 8 and 9 display the 3D views of cases b-1 to
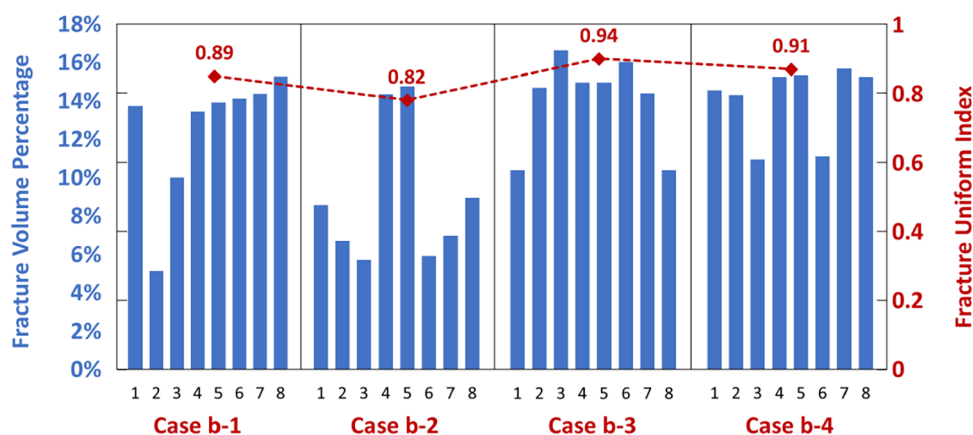
**Figure 9.** Distributions of fracture volume percentage and fracture uniformity indices of cases b-1 to b-4 with unevenly distributed cluster spacings, of which the spacing distribution modes are "5 | 5 | 8 | 8 | 12 | 12 | 15", "5 | 5 | 15 | 15 | 15 | 5 | 5", "5 | 8 | 12 | 15 | 12 | 8 | 5", and "5 | 15 | 5 | 15 | 5 | 15 | 5", respectively.
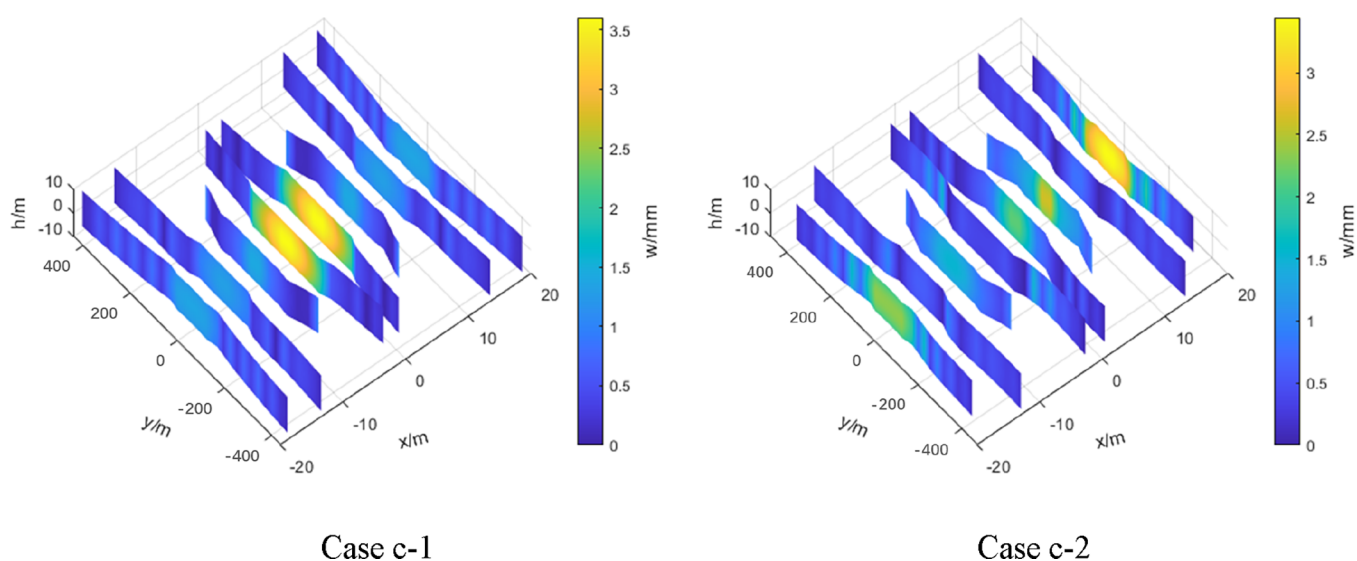


Case c-1                                    Case c-2

**Figure 10.** 3D views of case c-1 and case c-2 modeling results.
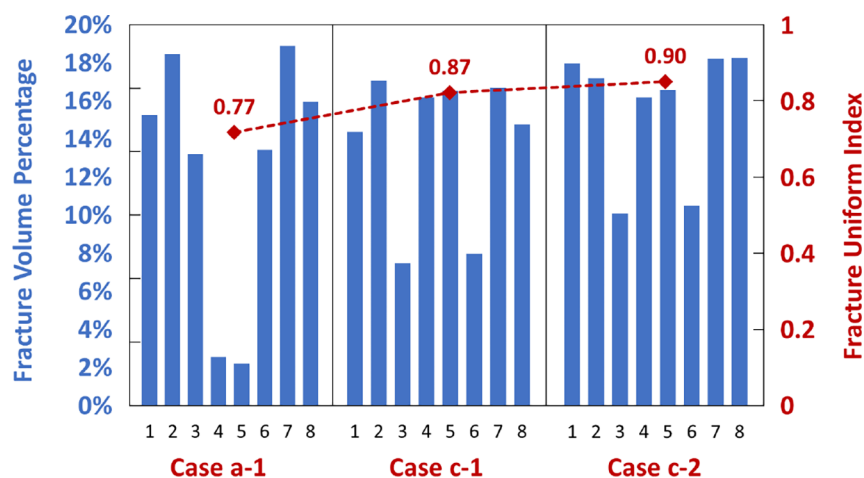


**Figure 11.** Fracture volume percentage distributions and fracture uniformity indices of cases a-1, c-1, and c-2 with the same cluster spacing of 5 m and even perforation numbers, of which the perforation numbers are 16, 8, and 4.

b-4 modeling results and the relationship between the distribution mode of cluster spacing and the fracture uniformity index $U_{fm}$, respectively, in which mode of case b-3 generates the

most uniform fractures ($U_{fm} = 0.94$) while the gradually increased arrangement mode of case b-1 results in the lowest uniformity ($U_{fm} = 0.89$). The increment of $U_{fm}$ between cases b-

Case c-3                    Case c-4
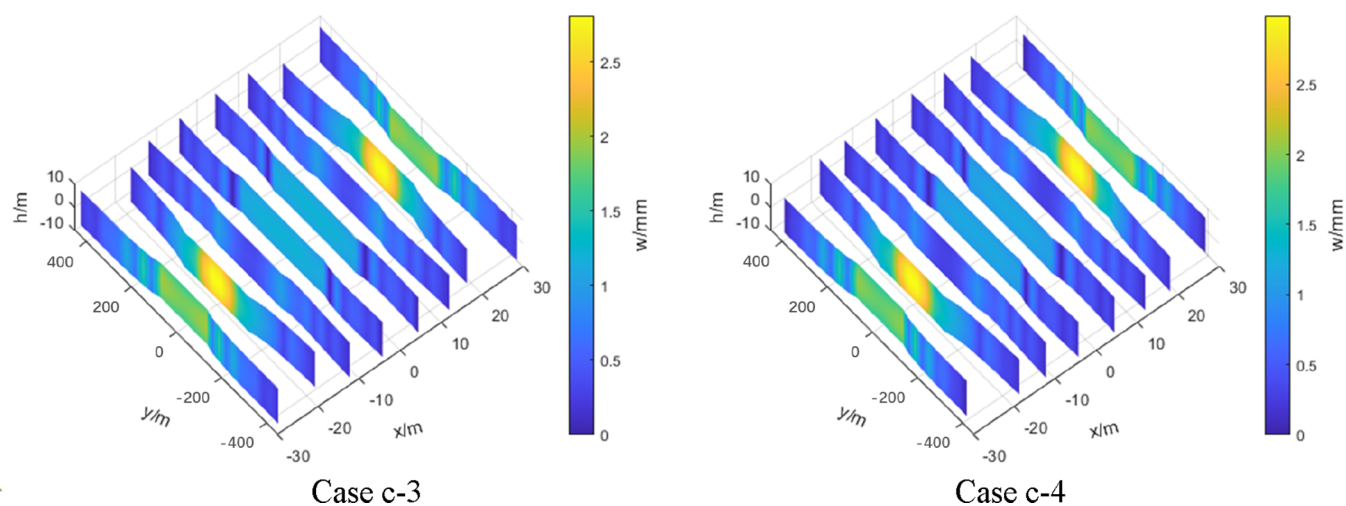
**Figure 12.** 3D views of cases c-3 to c-4 modeling results.



Case a-2          Case c-3          Case c-4
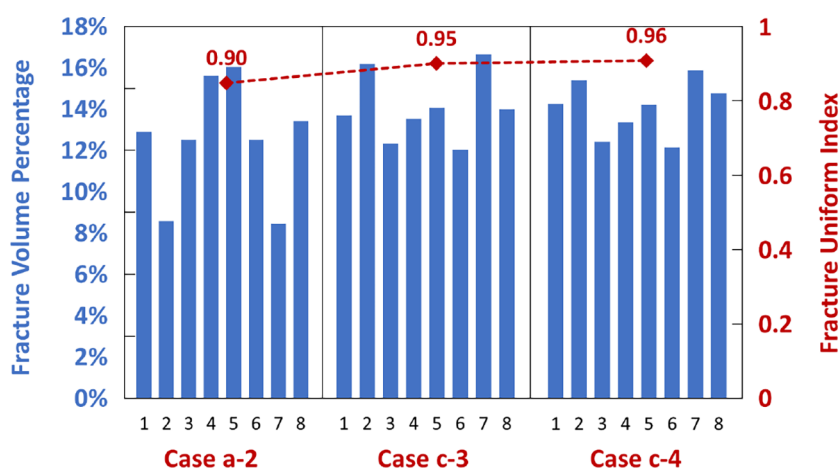
**Figure 13.** Fracture volume percentage distributions and fracture uniformity indices of cases a-2, c-3, and c-4 with the same cluster spacing of 8m and even perforation numbers, of which the perforation numbers are 16, 8, and 4.



Case d-1                    Case d-2                    Case d-3
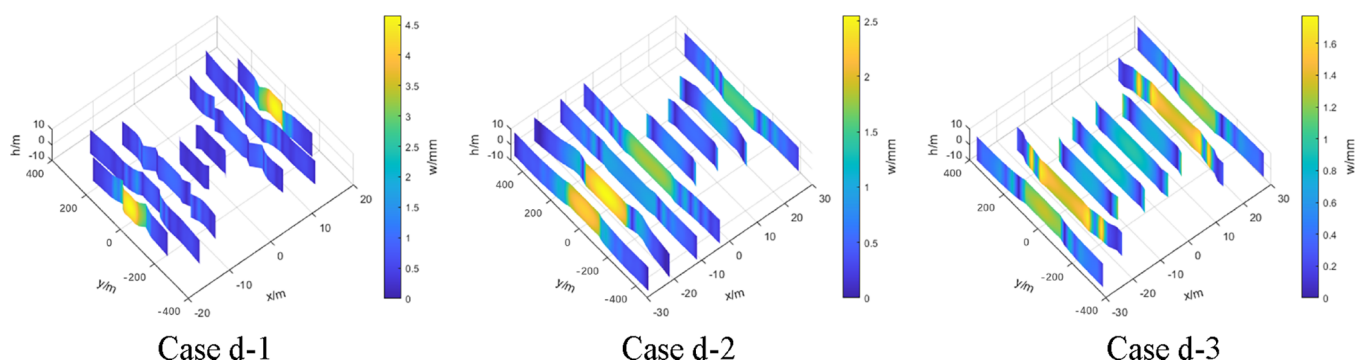
**Figure 14.** 3D views of cases d-1 to d-3 modeling results.

3 and b-1 is 5.6%. By comparing the "b" group (uneven-distributed cluster spacings) to the "a" group (even cluster spacings), it is hard to say there is an advantage for one group over the other one, but it can provide a reference for engineers to choose a spacing distribution pattern according the actual well log data and the demand of dense-segment. Taking an example of a horizontal well that has a general even TOC profile, the spacing mode of "decreasing from center to two sides" might be a good choice.

**3.3. Perforation Number.** First, cases of varied perforation numbers (case a-1, case c-1, and case c-2) are investigated, in which the cluster spacings are all set as even-distributed 5 m and the initial perforation diameters are all 7 mm. Figure 10 gives the modeling results of cases c-1 and c-2. Figure 11 displays the distribution of fracture volume percentages and the fracture uniformity indices of cases a-1, c-1, and c-2, which are set as 16, 8, and 4 perforations per cluster, respectively. It can be seen that the decreasing perforation number causes the increasing $U_{fm}$, and case c-2 with a perforation number of 4 perforations per
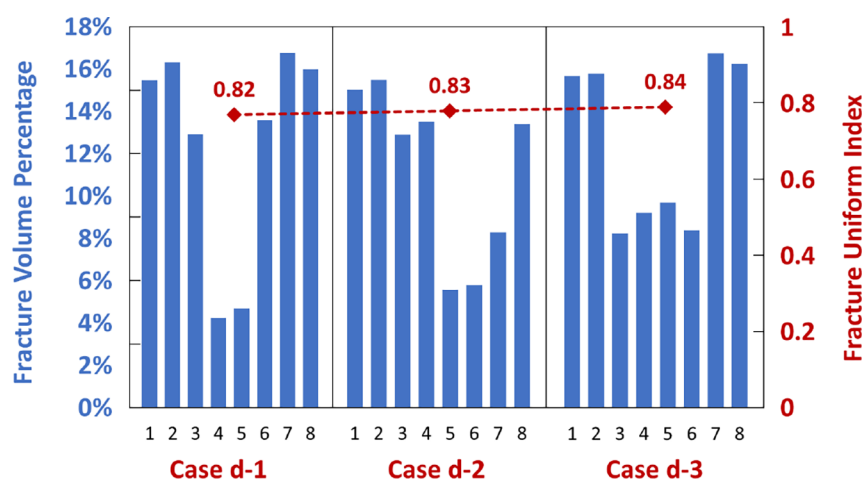
**Figure 15.** Fracture volume percentage distributions and fracture uniformity indices of cases d-1 to d-3 with the same cluster spacing of 8 m and uneven perforation numbers, of which the perforation number distribution modes are "2│2│2│3│3│4│4│4", "2│2│2│3│3│3│3│3│3", and "2│2│2│3│3│2│2│2", respectively.
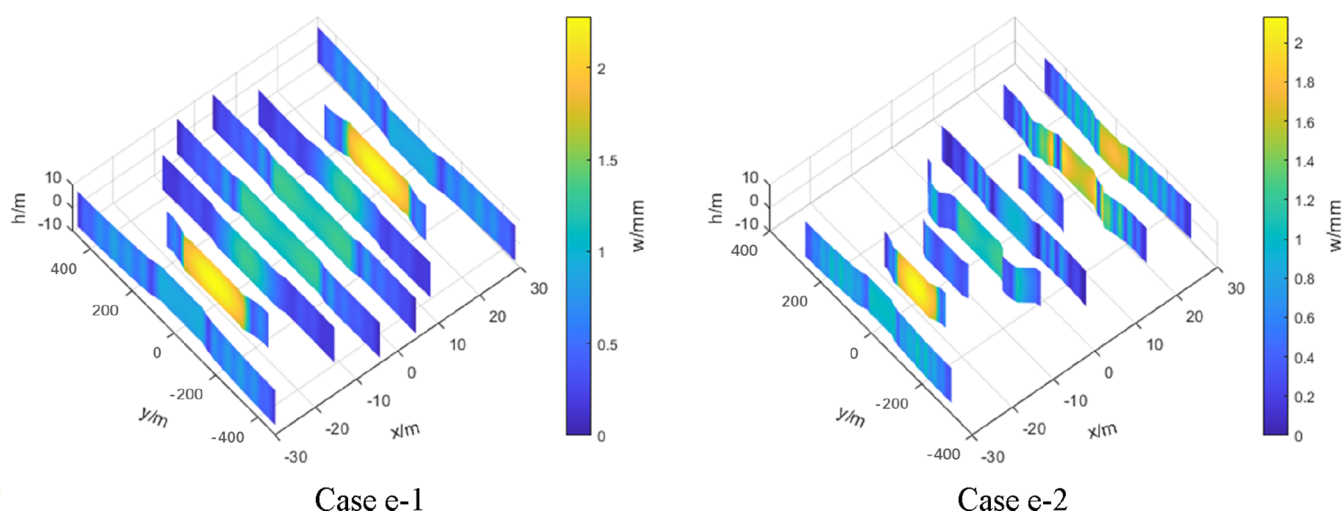


**Figure 16.** 3D views of cases e-1 to e-2 modeling results.

cluster, which can be identified as a limited-entry perforating case, generates the most uniform fractures. Under the condition of dense-segment perforation, the $U_{fm}$ of case c-2 is 16.9% over that of case a-1. It can be explained in eq 4 that the pressure difference between the casing pipe and the fracture would be improved as the perforation number is limited, which could positively balance the injection volume of fracturing fluid into each fractures. Another group of cases with larger even cluster spacings of 8m are analyzed (Figures 12 and 13) as well, and likewise the limited-entry perforating case c-4 with 4 perforation number per cluster has the highest $U_{fm}$. The $U_{fm}$ of case c-4 is 6.7% over that of case a-2. In this way, as the cluster spacing increases, the benefit of limiting the perforation number would shrink.

In addition, the uneven distribution modes of perforation number under the extreme limited-entry condition are analyzed. Cases d-1, d-2, and d-3 are taken as a group, and all the cases are set an average perforation number of around 3 perforations per cluster, respectively. Figure 14 presents the 3D views of cases d-1 to d-3 modeling results. In case d-1, the perforation number is set in a general increasing order from the toe side to the heel side, which is "2 _ 2 _ 2 _ 3 _ 3 _ 4 _ 4 _ 4". In case d-2, only the clusters of one side are perforated in a lower number than those

else, which is "2 _ 2 _ 2 _ 3 _ 3 _ 3 _ 3 _ 3 _ 3". While in case d-3, perforations are arranged in the mode of "more in center but fewer at sides", which is "2 _ 2 _ 2 _ 3 _ 3 _ 2 _ 2 _ 2". The fracture volume percentage distribution and fracture uniformity index $U_{fm}$ are displayed in Figure 15, from which it can be found that case d-3 has the highest $U_{fm}$, but only 2.4% over the lowest that of case d-1. In addition, the $U_{fm}$ values of the "d" group, in which the perforation numbers are unevenly distributed, are averagely 11.4% lower than those of cases a-2, c-3, and c-4, which have evenly distributed perforation numbers. It is normal for a homogeneous reservoir model because the unevenly distributed perforation numbers can easily cause a high in-flow rate cluster with a superior differential pressure than others.

**3.4. Initial Perforation Diameter.** It is clear from eq 4) that the perforation diameter can be a factor whose variation will lead to the change of pressure difference between the casing pipe and the fracture in addition to the perforation number. In order to investigate the relationship between perforation the hole diameter and fracture uniformity index, the even distribution group of cases a-2, e-1, and e-2, as well as the uneven distribution group of cases f-1 to f-3, are both computed. Since the perforation diameter will be enlarged as a result of the hole erosion, the initial perforation diameter is applied in every cases
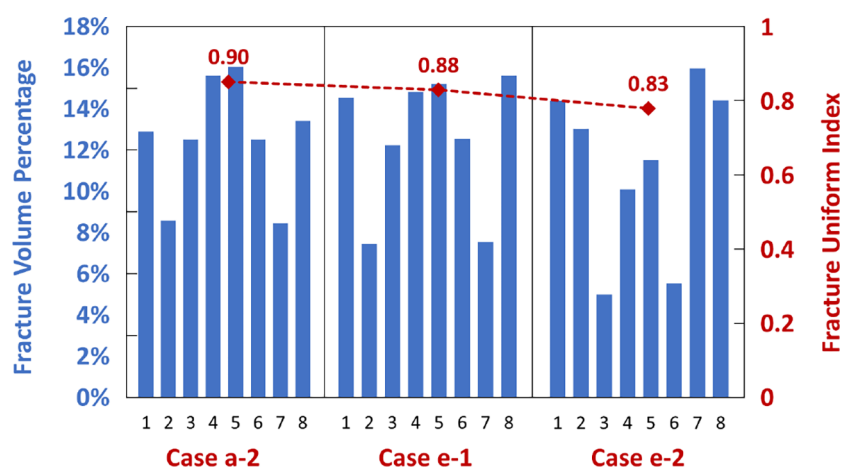
**Figure 17.** Fracture volume percentage distributions and fracture uniformity indices of cases a-1, e-1, and e-2 with the same cluster spacing of 8 m, the same perforation number of 16 per cluster, and even initial perforation diameters, of which the initial perforation diameters are 7, 10, and 14 mm, respectively.
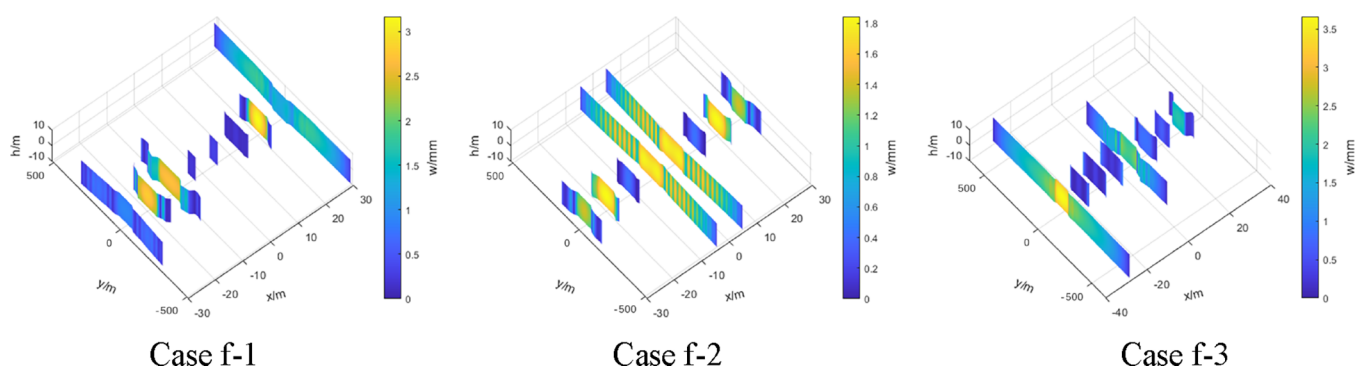


**Figure 18.** 3D views of cases d-1 to d-3 modeling results.
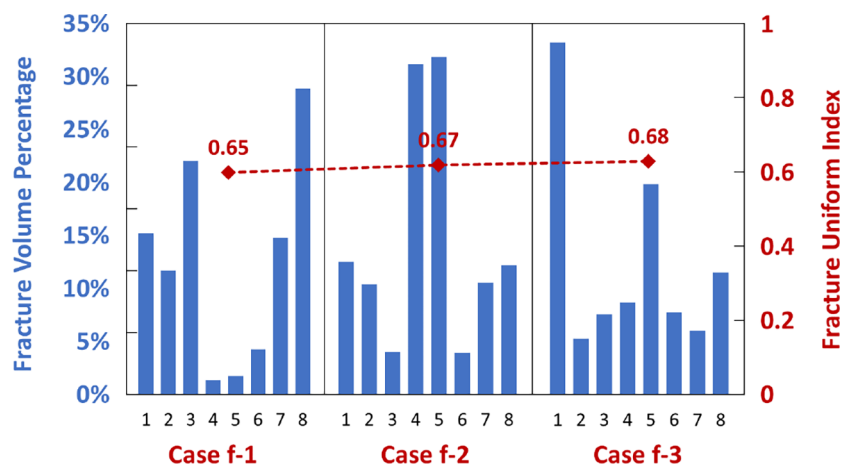


**Figure 19.** Fracture volume percentage distributions and fracture uniformity indices of cases f-1 to f-3 with the same cluster spacing of 8 m, the same perforation number of 16 per cluster, and uneven initial perforation diameters, of which the distribution modes of initial perforation diameters are "7 _ 7 _ 7 _ 14 _ 14 _ 7 _ 7 _ 7", "14 _ 14 _ 14 _ 7 _ 7 _ 14 _ 14 _ 14" and "7 _ 7 _ 7 _ 10 _ 10 _ 14 _ 14", respectively, and the units are all "mm".

instead of the dynamic perforation diameter value. The perforation diameters set for cases e-1 and e-2 are 10 and 14 mm. The distribution modes of perforation diameters applied in cases f-1 to f-3 are "large in center but small at sides" mode, "small in center but large at sides" mode, and "general increasing from toe side to heel side" mode, which are "7 _ 7 _ 7 _ 14 _ 14 _ 7 _ 7 _ 7", "14 _ 14 _ 14 _ 7 _ 7 _ 14 _ 14 _ 14", and "7 _ 7 _ 7 _ 10 _ 10 _ 14 _ 14 _ 14", respectively. In the even distribution

group, as shown in Figures 16 and 17, $U_{fm}$ changes in a negative correlation with the initial perforation diameter. The $U_{fm}$ value of case e-2 is 7.8% lower than that of case a-2. In the uneven distribution group, as shown in Figures 18 and 19, case f-1 gets the lowest $U_{fm}$, which is arranged with the most uneven initial perforation diameters. The $U_{fm}$ of case f-1 is 4.4% lower than that of case f-3, and the average $U_{fm}$ of "f" group is 23.4% lower than that of cases a-2, e-1, and e-2. The simulation results on various
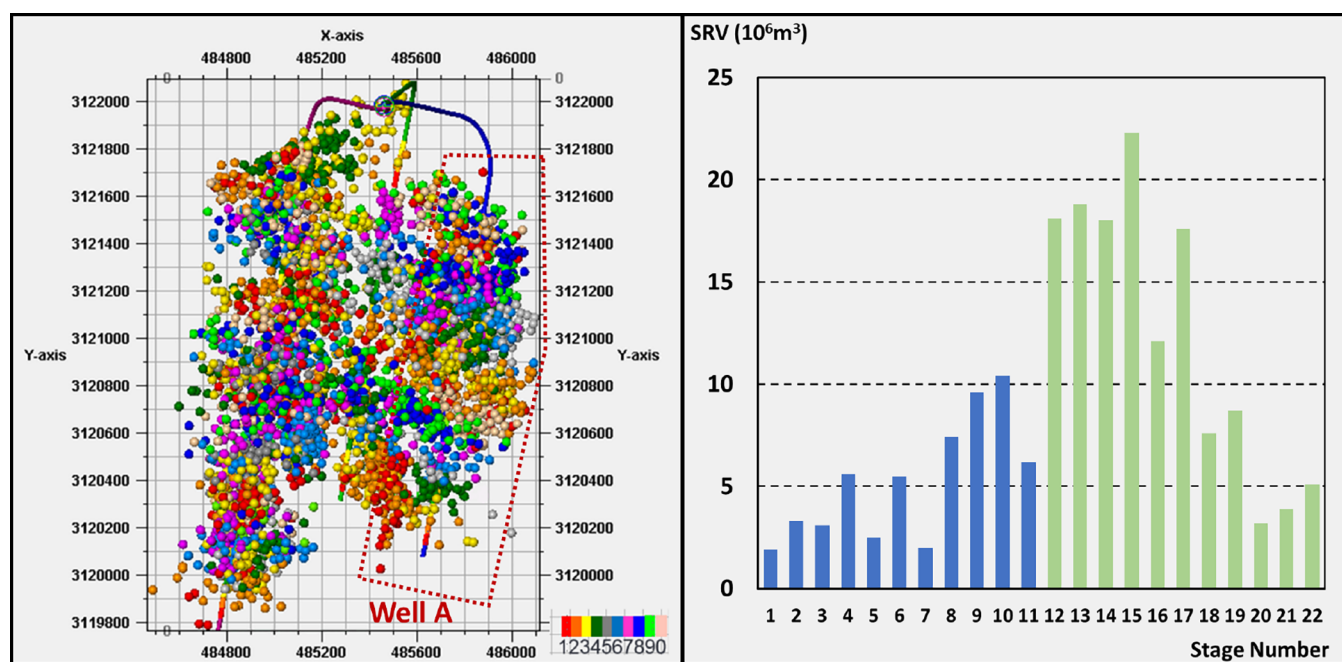
**Figure 20.** Fracture microseismic monitoring result and interpreted SRV statistical chart of well A1

initial perforation diameters indicate that it would be better to apply the single perforating charge in small size under a certain condition in order to gain a fracturing result of high uniformity.

## 4. FIELD APPLICATION

Well A was chosen as the application well of the perforation optimization method in this paper. Wells B, C, D, E, and F were the horizontal producing wells adjacent to well A in the same field (reservoir Y). The designed fracturing section of well A was 1647 m long, with 22 fracturing stages. The amount of fracturing fluid in a single stage was 1800 m$^3$, with an average fluid volume of 30.2 m$^3$/m and an average proppant mass of 3.1 t/m. The main pumping rate was controlled to not less than 14 m$^3$/min. In the actual perforation design progress, more related data were referred to such as TOC profile and brittleness index log, as a result of which, the optimized perforation parameters of each stage were mostly unevenly distributed. The field application of the perforation optimization method on well A achieved a success with good fracturing and postfrac production results.

**4.1. Microseismic Monitoring.** The stages no. 12–no. 22 of well A were selected as test stages to apply the perforation optimization method in this paper. On the one hand, the 11 test stages, all were treated by unevenly distributed perforation clusters with the average cluster spacing of 8 m under the principle of "dense-segment". On the other hand, the perforation number of each cluster was designed as a range of 2 to 4 by adopting the extreme limited-entry technique, and the actual perforation number at each cluster was decided by the breakdown pressure profile for a balanced injection rate as far as possible. The stages no. 1 to no. 11 of well A1 were empirically designed with even-distributed perforation parameters. Figure 20 demonstrates the microseismic monitoring result of the fractures and the interpreted SRV statistical chart of well A1. 3 gives the detailed treatment data and interpreted SRV of each stage in well A. It can be found that all the testing stages (no. 12 to no. 22) designed at the guidance of the perforation optimization method in this paper appear generally higher SRV values than the nontesting stages (no. 1 to no. 11), and the

**Table 3. Treatment Data and Interpreted SRV of Microseismic Events of Well A1**

| stage | injection rate (m$^3$/min) | treating pressure (MPa) | fluid volume (m$^3$) | proppant mass (t) | SRV (10$^6$ m$^3$) |
|---|---|---|---|---|---|
| 1 | 11–13.5 | 76–80 | 1935.9 | 180.12 | 1.9 |
| 2 | 14 | 70–73 | 1877 | 135.37 | 3.3 |
| 3 | 14 | 75–80 | 1996.7 | 196.38 | 3.1 |
| 4 | 14 | 70–76 | 1981 | 205.47 | 5.6 |
| 5 | 12–14 | 76–84 | 1888.2 | 200.03 | 2.5 |
| 6 | 14 | 74–78 | 1878 | 205.29 | 5.5 |
| 7 | 14 | 74–80 | 1923 | 202.52 | 2 |
| 8 | 14 | 71–75 | 1986 | 200 | 7.4 |
| 9 | 14 | 74–76 | 2096 | 200.02 | 9.6 |
| 10 | 14 | 71–73 | 1816.5 | 221.17 | 10.4 |
| 11 | 14 | 72–75 | 1981.2 | 200.08 | 6.2 |
| 12 | 14 | 72–75 | 1979.6 | 182.24 | 18.1 |
| 13 | 14 | 70–73 | 1975.5 | 210.3 | 18.8 |
| 14 | 14 | 70–73 | 1990 | 210.06 | 18 |
| 15 | 14 | 70–73 | 2031.7 | 200.88 | 22.3 |
| 16 | 14 | 68–72 | 1957.3 | 210.57 | 12.1 |
| 17 | 14 | 69–74 | 2195.1 | 195.19 | 17.6 |
| 18 | 14 | 73–76 | 1938.5 | 210.03 | 7.6 |
| 19 | 14 | 69–72 | 1994 | 210.91 | 8.7 |
| 20 | 14 | 66–70 | 1817.5 | 210.21 | 3.2 |
| 21 | 14 | 65–67 | 1805.8 | 210.67 | 3.9 |
| 22 | 14 | 65–73 | 1988 | 206.74 | 5.1 |

average SRV of the testing stages is over twice that of the commonly treated stages.

**4.2. Postfrac Production.** The gas production performance of Well A for the first two years after hydraulic fracturing is shown in Figure 21. The average daily gas production rate of well A is 8.88 × 10$^4$ m$^3$ per day, and the cumulative gas production reached 6.32 × 10$^6$ m$^3$. The production data of well A indicates the capability of continuable and stable gas production. A
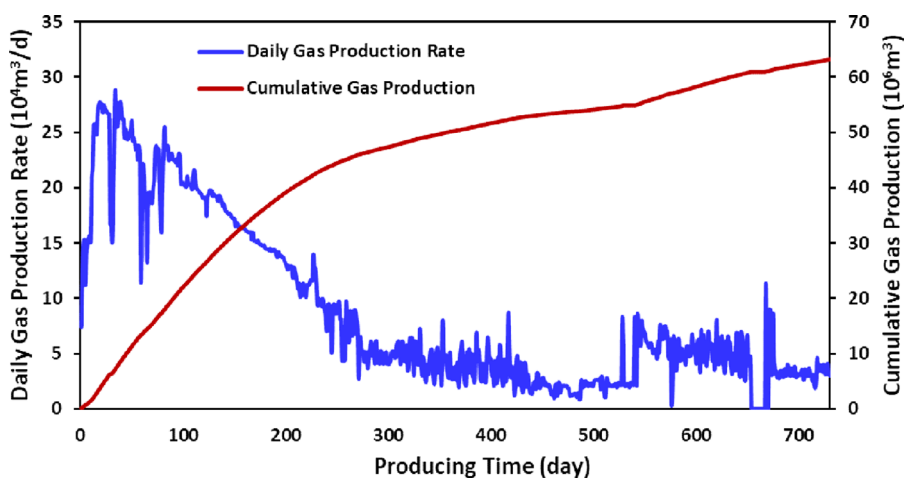
**Figure 21.** Daily gas production and cumulative gas production of well B.
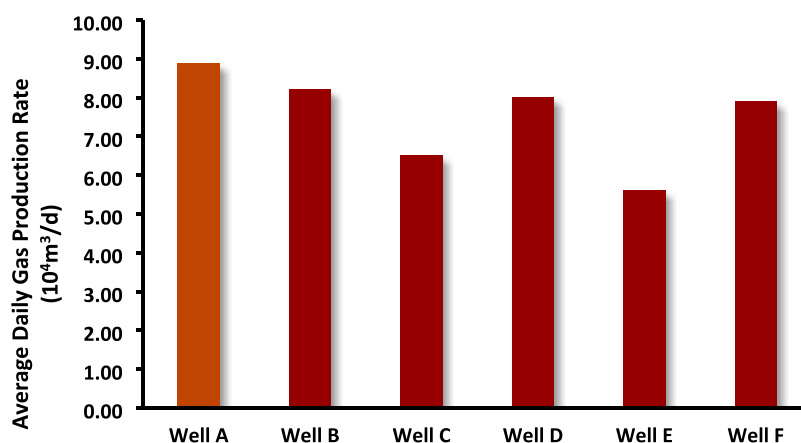


**Figure 22.** Average daily gas production rate of well A and adjacent wells.

comparison of the average daily gas production rate among well A and the five adjacent wells is illustrated in 22, from which it can be found that well A performs the most superior production capability.

## 5. CONCLUSIONS

In this study, we present a perforation optimization method for shale gas horizontal wells, utilizing pseudo-3D numerical simulations of multicluster fracturing. Our multicluster fracturing numerical model not only accommodates the fundamental functions of simultaneous fracture propagations and balance in inflow rates but also incorporates the hole erosion process and considers the initiation asynchrony effect. Furthermore, we investigate the influencing patterns of cluster spacing, perforation number, and initial perforation diameter on the fracture propagation uniformity index by analyzing simulation results from 20 cases with varying input perforation parameters. The expression for the fracture propagation uniformity index is modified to account for the impact of the total number of fractures.

Based on the numerical modeling results and case discussions, we derive theoretical guidance for optimizing perforation parameters to achieve uniform fracture propagation in multicluster fracturing wells:

a) Under basic design requirements, it is recommended to arrange cluster spacings in a distribution mode of "circulation with a large one and a small one," with an average cluster spacing as large as possible.

b) While ensuring satisfaction of provided pumping pressure, adopting a limited-entry or extreme limited-entry design helps improve fracture propagation uniformity. However, the distribution mode of perforation numbers depends on well log data such as TOC profile and brittleness index log.

c) In cases where a certain cluster exhibits an easily biased inflow rate and poor fracture propagation uniformity, a small perforation hole is recommended.

The interpreted fracturing results and postfracturing production data from well A validate the feasibility of the perforation optimization method outlined in this paper for enhancing fracture uniformity. Nevertheless, the practical field presents challenges due to highly heterogeneous rock properties and complex natural fractures, which impact the accuracy of perforation parameter optimization. As engineers continue to seek advancements in reservoir stimulation and well completion, there exists substantial potential for functional evolution in the numerical simulation of hydraulic fracturing. Moreover, enriching the number of cases exploring the relationship between the perforation parameters and fracturing results is essential.

## AUTHOR INFORMATION

### Corresponding Authors

**Chang Liu** − *State Key Laboratory of Oil and Gas Reservoir Geology and Exploitation, Southwest Petroleum University, Chengdu 610500, China;* orcid.org/0009-0000-9992-8295; Email: redlc123@hotmail.com

**Ying Li** − *State Key Laboratory of Oil and Gas Reservoir Geology and Exploitation, Southwest Petroleum University, Chengdu 610500, China;* Email: yingingli@163.com

### Authors

**Haitao Li** − *State Key Laboratory of Oil and Gas Reservoir Geology and Exploitation, Southwest Petroleum University, Chengdu 610500, China*

**Hongwen Luo** − *State Key Laboratory of Oil and Gas Reservoir Geology and Exploitation, Southwest Petroleum University, Chengdu 610500, China*

**Yu Lu** − *Chongqing University of Science and Technology, Chongqing 401331, China;* orcid.org/0000-0001-9810-9255

**Chao Su** − *Geological Exploration and Development Research Institute, Chuanqing Drilling Engineering Company, Chengdu 610051, China*

**Shengnan Chen** − *Department of Chemical and Petroleum Engineering, Schulich School of Engineering, University of Calgary, Calgary T2N 1N4, Canada;* orcid.org/0000-0002-1704-1007

Complete contact information is available at:
https://pubs.acs.org/10.1021/acsomega.3c06416

### Notes

The authors declare no competing financial interest.

## REFERENCES

(1) Detournay, E. Mechanics of Hydraulic Fractures. *Annu. Rev. Fluid Mech.* **2016**, *48* (1), 311−339, DOI: 10.1146/annurev-fluid-010814-014736.

(2) Adachi, J.; Siebrits, E.; Peirce, A.; Desroches, J. Computer simulation of hydraulic fractures. *Int. J. Rock Mech. Min. Sci.* **2007**, *44* (5), 739−757.

(3) Carrier, B.; Granet, S. Numerical modeling of hydraulic fracture problem in permeable medium using cohesive zone model. *Engineering Fracture Mechanics* **2012**, *79*, 312−328.

(4) Wang, T.; Zhou, W. B.; Chen, J. H.; Xiao, X.; Li, Y.; Zhao, X. Y. Simulation of hydraulic fracturing using particle flow method and application in a coal mine. *International Journal of Coal Geology* **2014**, *121*, 1−13.

(5) Zuo, K.; Yang, J.; Luo, H.; Haitao, Li; Xiang, Y.; Li, Y.; Jiang, B.; Nie, S.; Zhang, Q. An efficient inversion method to interpret distributed temperature measurement of horizontal wells in shale gas reservoirs. *Pet. Sci. Technol.* **2023**, 1−22.

(6) Dong, C. Y.; de Pater, C. J. Numerical implementation of displacement discontinuity method and its application in hydraulic fracturing. *Comput. Methods Appl. Mech. Eng.* **2001**, *191* (8-10), 745−760.

(7) Yang, W.; Lv, X.; Wang, L.; Peng, D.; Chen, X. A DEM−CFD coupling method for modelling two-hole synchronous hydraulic fracturing. *Geomech. Geophys. Geo-Energy Geo-Resour.* **2023**, *9* (1), 6 DOI: 10.1007/s40948-023-00556-w.

(8) Cai, J.; Li, F. Estimation of Fracture Height in Tight Reservoirs via a Finite Element Approach. *Processes* **2023**, *11* (5), 1566 DOI: 10.3390/pr11051566.

(9) Mou, P.; Pan, J.; Wang, K.; Wei, J.; Yang, Y.; Wang, X. Influences of hydraulic fracturing on microfractures of high-rank coal under different in-situ stress conditions. *Fuel* **2021**, *287*, No. 119566.

(10) Wang, X.; Pan, J.; Wang, K.; Mou, P.; Li, J. Fracture variation in high-rank coal induced by hydraulic fracturing using X-ray computer tomography and digital volume correlation. *International Journal of coal geology* **2022**, *252*, No. 103942.

(11) Duan, K.; Kwok, C. Y.; Zhang, Q.; Shang, J. On the initiation, propagation and reorientation of simultaneously-induced multiple hydraulic fractures. *Comput. Geotech.* **2020**, *117*, No. 103226.

(12) Duan, K.; Kwok, C. Y.; Wu, W.; Jing, L. DEM modeling of hydraulic fracturing in permeable rock: influence of viscosity, injection rate and in situ states. *Acta Geotech.* **2018**, *13*, 1187 DOI: 10.1007/s11440-018-0627-8.

(13) Zhang, F. S.; Damjanac, B.; Maxwell, S. Investigating Hydraulic Fracturing Complexity in Naturally Fractured Rock Masses Using Fully Coupled Multiscale Numerical Modeling. *Rock Mechanics and Rock Engineering* **2019**, *52* (12), 5137−5160.

(14) King, G. E. 60 Years of Multi-Fractured Vertical, Deviated and Horizontal Wells: What Have We Learned? In *SPE Annual Technical Conference and Exhibition.* SPE 2014 DOI: 10.2118/170952-MS.

(15) Wheaton, B.; Haustveit, K.; Deeg, W.; Miskimins, J.; Barree, R. A Case Study of Completion Effectiveness in the Eagle Ford Shale Using DAS/DTS Observations and Hydraulic Fracture Modeling. In *SPE Hydraulic Fracturing Technology Conference.* 2016 SPE DOI: 10.2118/179149-MS.

(16) Li, Y.; Deng, J. G.; Liu, W.; Yan, W.; Feng, Y. C.; Cao, W. K.; Wang, P. F.; Hou, Y. L. Numerical simulation of limited-entry multi-cluster fracturing in horizontal well. *J. Pet. Sci. Eng.* **2017**, *152*, 443−455.

(17) Luo, H.; Li, H.; Lu, Y.; Li, Y.; Guo, Z. Inversion of distributed temperature measurements to interpret the flow profile for a multistage fractured horizontal well in low-permeability gas reservoir. *Applied Mathematical Modelling* **2020**, *77*, 360−377.

(18) Luo, H.; Li, H.; Li, Y.; Lu, Y.; Tan, Y. Investigation of temperature behavior for multi-fractured horizontal well in low-permeability gas reservoir. *Int. J. Heat Mass Transfer* **2018**, *127*, 375−395.

(19) Luo, H.; Li, H.; Tan, Y.; Li, Y.; Jiang, B.; Lu, Y.; Cui, X. A novel inversion approach for fracture parameters and inflow rates diagnosis in multistage fractured horizontal wells. *J. Pet. Sci. Eng.* **2020**, *184*, No. 106585.

(20) Hongwen, L.; Haitao, L.; Ying, Li; Feng, W.; Yuxing, X.; Beibei, J.; Hao, Y. Inversion and interpretation of production profile and fracture parameters of fractured horizontal wells in low-permeability gas reservoirs. *Acta Pet. Sin.* **2021**, *42* (7), 936−947.

(21) Li, H.; Luo, H.; Xiang, Y.; Li, Y.; Jaing, B.; Cui, X.; Gao, S.; Zou, S.; Xin, Y. DTS based hydraulic fracture identification and production profile interpretation method of horizontal shale gas wells. *Nat. Gas Ind. B* **2021**, *8* (5), 494−504.

(22) Wei, C.; Liu, Y.; Deng, Y.; Cheng, S.; Hassanzadeh, H. Temperature Transient Analysis of Naturally Fractured Geothermal Reservoirs. *SPE J.* **2022**, *27*, 2723−2745.

(23) Miller, C., Waters, G., Rylander, E. Evaluation of production log data from horizontal wells drilled in organic shales. In *SPE Unconventional Resources Conference/Gas Technology Symposium.* 2011. SPE DOI: 10.2118/144326-MS.

(24) Cipolla, C., Weng, X.; Onda, H.; Nadaraja, T.; Malpani, R. New Algorithms and Integrated Workflow for Tight Gas and Shale Completions. In *SPE Annual Technical Conference & Exhibition.* 2011 SPE-146872 SPE DOI: 10.2118/146872-MS.

(25) Luo, H.; Li, Y.; Li, H.; Cui, X.; Chen, Z. Simulated annealing algorithm-based inversion model to interpret flow rate profiles and

fracture parameters for horizontal wells in unconventional gas reservoirs. *SPE Journal* **2021**, *26* (04), 1679−1699.

(26) Wutherich, K. D.; Walker, K. J. Designing Completions in Horizontal Shale Gas Wells - Perforation Strategies. 2012, In *SPE Unconventional Resources Conference/Gas Technology Symposium*, SPE-155485-MS SPE DOI: 10.2118/155485-MS.

(27) Nagel, N. B.; Sanchez-Nagel, M. Stress shadowing and microseismic events: a numerical evaluation. In *SPE Annual Technical Conference and Exhibition*. 2011, SPE Denver, Colorado, USA DOI: 10.2118/147363-MS.

(28) Guo, J.; Lu, Q.; Zhu, H.; Wang, Y.; Ma, L. Perforating cluster space optimization method of horizontal well multi-stage fracturing in extremely thick unconventional gas reservoir. *Journal of Natural Gas Science and Engineering* **2015**, *26*, 1648−1662.

(29) Zhao, J.; Chen, X.; Li, Y.; Fu, B. Simulation of simultaneous propagation of multiple hydraulic fractures in horizontal wells. *J. Pet. Sci. Eng.* **2016**, *147*, 788−800.

(30) Wang, H. Numerical investigation of fracture spacing and sequencing effects on multiple hydraulic fracture interference and coalescence in brittle and ductile reservoir rocks. *Engineering Fracture Mechanics* **2016**, *157*, 107−124.

(31) Crump, J.; Conway, M. Effects of perforation-entry friction on bottomhole treating analysis. *Journal of petroleum technology* **1988**, *40* (08), 1041−1048.

(32) Lecampion, B.; Desroches, J. Robustness to formation geological heterogeneities of the limited entry technique for multi-stage fracturing of horizontal wells. *Rock Mech. Rock Eng.* **2015**, *48*, 2637 DOI: 10.1007/s00603-015-0836-5.

(33) Daneshy, A. Dynamic Interaction Within Multiple Limited Entry Fractures in Horizontal Wells: Theory, Implications, and Field Verification. In *SPE Hydraulic Fracturing Technology Conference*. 2015 SPE-173344-MS SPE DOI: 10.2118/SPE-173344-MS.

(34) Desroches, J., Lecampion, B.; Ramakrishnan, H.; Prioul, R.; Brown, J. E. Benefits of Controlled Hydraulic Fracture Placement: Theory and Field Experiment. In *SPE/CSUR Unconventional Resources Conference − Canada - Calgary, Alberta, Canada* 2014 D011S003R004 SPE DOI: 10.2118/171667-MS.

(35) Lecampion, B., Desroches, J.; Weng, X.; Burghardt, J.; Brown, J. E. Can We Engineer Better Multistage Horizontal Completions? Evidence of the Importance of Near-Wellbore Fracture Geometry From Theory, Lab and Field Experiments. In *SPE Hydraulic Fracturing Technology Conference* 2015 D021S003R001 SPE DOI: 10.2118/SPE-173363-MS.

(36) Li, Y.; Deng, J.; Liu, W.; Yan, W.; Feng, Y.; Cao, W.; Wang, P.; Hou, Y. Numerical Simulation of Limited-Entry Multi-Cluster Fracturing in Horizontal Well. *J. Pet. Sci. Eng.* **2017**, *152*, 443−455.

(37) Lu, Y.; Li, H.; Lu, C.; Wu, K.; Chen, Z.; Wang, K.; Luo, H.; Shan, J. The effect of completion strategy on fracture propagation from multiple cluster perforations in fossil hydrogen energy development. *Int. J. Hydrogen Energy* **2019**, *44* (14), 7168−7180.

(38) Wu, K.; Olson, J. E. Simultaneous Multifracture Treatments: Fully Coupled Fluid Flow and Fracture Mechanics for Horizontal Wells. *SPE Journal* **2015**, *20* (2), 337−346.

(39) Lecampion, B.; Bunger, A.; Zhang, X. Numerical methods for hydraulic fracture propagation: A review of recent trends. *Journal of Natural Gas Science and Engineering* **2018**, *49*, 66−83.

(40) Carter, R. Derivation of the General Equation for Estimating the Extent of the Fractured Area. Appendix to Optimum Fluid Characteristics for Fracture Extension, GC Howard and CR Fast, Drilling and Production Practice, New York City, New York, USA, 1 January. *Drill. Prod. Prac.* **1957**, 261−270.

(41) Lamb, A. R.; Gorman, G. J.; Elsworth, D. A fracture mapping and extended finite element scheme for coupled deformation and fluid flow in fractured porous media. *International Journal for Numerical and Analytical Methods in Geomechanics* **2013**, *37* (17), 2916−2936.

(42) Barenblatt, G. I.; Zheltov, Y. P.; Kochina, I. N. Basic Concepts in the Theory of Seepage of Homogeneous Liquids in Fissured Rocks. *J. Appl. Math.* **1960**, *24* (5), 5−1303.

(43) Elbel, J. L., Piggott, A. R., Mack, M. G. Numerical modeling of multilayer fracture treatments. In *SPE Permian Basin Oil and Gas Recovery Conference*. 1992. SPE DOI: 10.2118/23982-MS.

(44) Valkó, P., Economides, M. J. *Hydraulic fracture mechanics*. Vol. 28, 1995, Wiley Chichester.

(45) Crouch, S. L.; Starfield, A.M.; Rizzo, F. Boundary element methods in solid mechanics. *J. Appl. Mech.* **1983**, *50*, 704 DOI: 10.1115/1.3167130.

(46) Olson, J. E. Predicting fracture swarms—The influence of subcritical crack growth and the crack-tip process zone on joint spacing in rock. *Geological Society, London, Special Publications* **2004**, *231* (1), 73−88.

(47) Olson, J. E. *Fracture mechanics analysis of joints and veins*. 1991, Stanford University.

(48) Olson, J. Fracture aperture, length and pattern geometry development under biaxial loading: a numerical study with applications to natural, cross-jointed systems. *Geological Society, London, Special Publications* **2007**, *289* (1), 123−142.

(49) Erdogan, F.; Sih, G. On the crack extension in plates under plane loading and transverse shear. *J. Basic Eng.* **1963**, *85*, 519−527.

(50) Hossain, M. M., Rahman, M.K., Rahman, S.S. Volumetric Growth and Hydraulic Conductivity of Naturally Fractured Reservoirs During Hydraulic Fracturing: A Case Study Using Australian Conditions. In *SPE Annual Technical Conference and Exhibition*. 2000 SPE-63173 SPE DOI: 10.2118/63173-MS.

(51) Long, G.; Liu, S.; Xu, G.; Wong, S.W.; Chen, H.; Xiao, B. A Perforation-Erosion Model for Hydraulic-Fracturing Applications. *SPE Prod. Oper.* **2018**, *33*, 770 DOI: 10.2118/174959-PA.

(52) Cramer, D., Friehauf, K.; Roberts, G.; Whittaker, J. Integrating DAS, treatment pressure analysis and video-based perforation imaging to evaluate limited entry treatment effectiveness. In *SPE Hydraulic Fracturing Technology Conference and Exhibition*. 2019. SPE-194334-MS SPE DOI: 10.2118/194334-MS.

(53) Barree, R. D. Potential Issues with Extreme Limited Entry in Horizontal Wells. In *SPE/AAPG/SEG Unconventional Resources Technology Conference*. 2020. Unconventional Resources Technology Conference (URTEC) OnePetro DOI: 10.15530/urtec-2020-1024.

(54) Horton, B. A Shot in the Dark: How Your Post-Fracture Perforation Imaging can be Misleading and How to Better Understand Cluster Efficiency and Optimize Limited Entry Perforating. in *SPE Hydraulic Fracturing Technology Conference and Exhibition*. 2021. SPE-204177-MS OnePetro DOI: 10.2118/204177-MS.

(55) Peirce, A. P.; Bunger, A. P. Interference fracturing: nonuniform distributions of perforation clusters that promote simultaneous growth of multiple hydraulic fractures. *SPE Journal* **2015**, *20* (02), 384−395.

(56) Lu, Q. Unconventional reservoir perforating cluster spacing optimization method for staged-fracturing horizontal well. In *SPE Annual Technical Conference and Exhibition*. 2016. SPE-184483-STU SPE DOI: 10.2118/184483-STU.